

ADA 087043

LEVEL

②

14
PSR Report 923

6
MULTIPLE SCATTERING IN CLOUDS

10 A. P. Ciervo

11 Sep 1979

12 78

DTIC
ELECTE
JUL 23 1980
S D

16 RF21226

17 RF21222801

Final Report
Contract No. N00014-78-C-0751

15 DARPA Order -
3650

Sponsored by
Office of Naval Research
800 North Quincy Street
Arlington, Virginia 22217

APPROVED FOR PUBLISHING RELEASE
DISTRIBUTION UNLIMITED

The Ruth H. Hooker Technical Library

OCT 16 1979

Naval Research Laboratory



PACIFIC SIERRA RESEARCH CORP.

DDC FILE COPY

80

407486

7

22

11

PREFACE

This report presents a new analytic approach to optical pulse propagation through a multiple scattering medium. Such a model is needed to resolve propagation issues in the Blue-Green Optical Communication Program. The analytic model is capable of (1) duplicating highly aggregated Monte Carlo computations at significantly lower cost, and (2) providing detailed computations (e.g., involving finite-dimension receivers) that are impractical to simulate.

The effort was jointly funded by the Defense Advanced Research Projects Agency, the Office of Naval Research, and the Naval Electronics System Command. The technical advisor was the Naval Ocean Systems Center. The report should be immediately useful for verifying or updating modular expressions in the current Navy model for single-pulse downlink propagation.

W
D
S
EL
JUL 23 1980
D
C

APPROVED FOR PUBLISHING DETAILS
DISTANCE FROM ORIGIN

Accession for	
MTA	<input checked="checked" type="checkbox"/>
DDC	<input type="checkbox"/>
Unpublished	<input type="checkbox"/>
Justification	
By _____	
Distribution/	
Availability Codes	
Dist	Avail and/or special
A	

ABSTRACT

✓

This report develops an analytic model for the propagation of an optical pulse through a multiple scattering medium. Such a model is needed to investigate the effect of clouds on optical communications from a satellite to a submarine. A key initial result is the derivation of simple expressions for the first two spatial and angular moments of the radiance distribution for a narrow delta-function source immersed in an infinite scattering medium. The moments support a diffusion approximation for the transport process in an infinite plane-parallel cloud. First the radiance is calculated at the cloud exit and on a plane an arbitrary distance below the cloud, then power collected by a finite receiver located on this plane is computed. The model is validated by comparing its results with computer simulation curve fits for optically thick clouds (i.e., $\tau > 15$). The model is capable of duplicating nearly all the simulation results but at significantly lower cost. Furthermore, detailed calculations impractical to simulate are readily computed.

↑ TAU

ACKNOWLEDGMENTS

The author is indebted to G. J. Hall for the initial derivation of the moment formulae, and to D. E. Snead for subsequent refinements. R. F. Lutomirski and R. E. Warren provided valuable insights and encouragement throughout the effort.

The author is also grateful for the financial support and technical direction of M. White and D. Lewis of the Office of Naval Research, Commander T. Weiner of the Defense Advanced Research Projects Agency, and M. L. Parker, Jr., of the Naval Electronics System Command. The technical advice provided by L. B. Stotts of the Naval Ocean Systems Center ensured the relevance of the research to the Blue-Green Optical Communication Program.

CONTENTS

PREFACE	iii
ABSTRACT	v
ACKNOWLEDGMENTS	vii
FIGURES	xi
Section	
I. INTRODUCTION AND SUMMARY	1
II. MOMENTS OF RADIANCE DISTRIBUTION	5
Conditional Mean $\bar{\underline{x}}_n(\xi)$	8
Conditional Second Moment $\langle \underline{x}_n(\xi) \underline{x}_n^T(\xi) \rangle$	10
Conditional Angular Moments $\langle \cos \theta \rangle_n$ and $\langle \cos^2 \theta \rangle_n$..	17
Unconditional Moments	18
III. MOMENT ILLUSTRATIONS AND ASYMPTOTICS	23
Diffusion Regime	23
Forward Scatter Regime	28
Conditional Moments	32
IV. DIFFUSION APPROXIMATION FOR MULTIPLE SCATTERING IN AN INFINITE CLOUD LAYER	35
Diffusion Equation	35
Boundary Conditions	37
Irradiance at Cloud Exit	41
Comparison with Monte Carlo Simulations	43
V. PROPAGATION BELOW CLOUD AND FINITE RECEIVER CALCULATIONS	52
Radiance and Received Power at Cloud Exit	53
Propagation Below Cloud	54
VI. IMPLICATIONS FOR BLUE-GREEN PROGRAM	66
Navy Model	67
Experimental Verification	68
REFERENCES	71

FIGURES

1. Propagation Path with Model Parameters	2
2. Scattering Geometry	6
3. Mean Photon Penetration Parameterized on $\langle \cos \theta \rangle$	24
4. Spatial Standard Deviations Plotted for $\langle \cos \theta \rangle =$ $\langle \cos^2 \theta \rangle = 0.850$	25
5. First Two Angular Moments for $\langle \cos \theta \rangle = \langle \cos^2 \theta \rangle = 0.850$	27
6. Effects of Small-Angle Assumption on rms Beam Spread	30
7. Average Multipath Time Delay for $\langle \cos \theta \rangle = 0.827$	31
8. Conditional Spatial Moments for $\langle \cos \theta \rangle = \langle \cos^2 \theta \rangle$ $= 0.850$	33
9. Representation of Photon Density $\rho_z(z, \xi)$, ξ Fixed, Using Diffusion Theory Approximation with Extended Cloud Boundary Condition	39
10. Comparison of Simulated and Calculated Power Pulses for $\tau = 30$	45
11. Comparison of Simulated and Calculated Power Pulses for $\tau = 80$	46
12. Comparison of Simulated and Calculated Energy Trans- mission Versus Optical Thickness for $\langle \cos \theta \rangle = 0.827$..	47
13. Comparison of Simulated and Calculated Mean Radial Distance of Emerging Photons Versus Optical Thick- ness for $\langle \cos \theta \rangle = 0.827$	49
14. Comparison of Simulated and Calculated Average Multi- path Time Delay Versus Optical Thickness for $\langle \cos \theta \rangle = 0.827$	51
15. Received Energy Versus Field of View Using a Generally Applicable Expression and One Restricted to Small- Field-of-View Receivers	59
16. Received Energy Versus Distance Below Cloud for $\tau = 30$ and Various Receiver Fields of View	60
17. Average Multipath Time Delay Versus Distance Below Cloud for $\tau = 30$ and Various Receiver Fields of View ..	61
18. Received Energy Versus Distance Below Cloud for 15° Field of View and Various Cloud Thicknesses	62
19. Multipath Time Delay Versus Distance Below Cloud for 15° Field of View and Various Cloud Thicknesses	63

20. Received Energy Versus Optical Thickness of Cloud for 15° Field of View and Various Receiver-to-Cloud Distances	64
21. Multipath Time Delay Versus Optical Thickness of Cloud for 15° Field of View and Various Receiver-to-Cloud Distances	65

I. INTRODUCTION AND SUMMARY

This report develops an analytic model for the propagation of an optical pulse through a multiple scattering medium. Such a model is needed to investigate the effect of clouds on satellite-to-submarine communications by means of a blue-green laser. Figure 1 shows the portion of the propagation path considered here as well as the key physical and system parameters of the environment and the receiver.

We consider both a narrow collimated and a broad Gaussian beam as a source function at the cloud entrance. In both cases, however, the source is assumed to be a delta function in time. The narrow beam response provides both a Green's function for the broad beam input and a tool for comparing our results with Monte Carlo simulations. The cloud is assumed to be a plane-parallel slab of infinite horizontal extent. Cloud parameters are physical thickness Z_0 , optical thickness τ , scattering coefficient k_s , single-scatter albedo λ , average cosine of the polar scattering angle $g = \langle \cos \theta \rangle$, and $\langle \cos^2 \theta \rangle$. We provide analytic expressions for the radiance at the cloud exit (i.e., at $z = \tau = k_s Z_0$) and the power received by an infinite plane receiver. The latter expression corresponds to the problem addressed by computer simulation experiments.

Figure 1 shows that the radiance emerging from the cloud is propagated through the atmosphere to a plane just above the ocean surface (i.e., $z = \tau + d$). The atmospheric layer below the cloud is characterized by its physical thickness Z_1 and absorption coefficient k_a ; the normalized distance d in Fig. 1 is given by $d = k_s Z_1$. We calculate the power into an on-axis receiver (at $z = \tau + d$) with aperture a and polar field-of-view half-angle θ_{fov} . In an actual communication link, the receiver would, of course, be located on a submarine some distance below the ocean surface. However, we calculate the received pulse above the ocean surface to develop modular expressions for transmission and pulse spreading due to clouds and atmosphere alone, and to enable experimental verification of our results with data gathered by ground-based receivers [1] or scaled laboratory experiments.

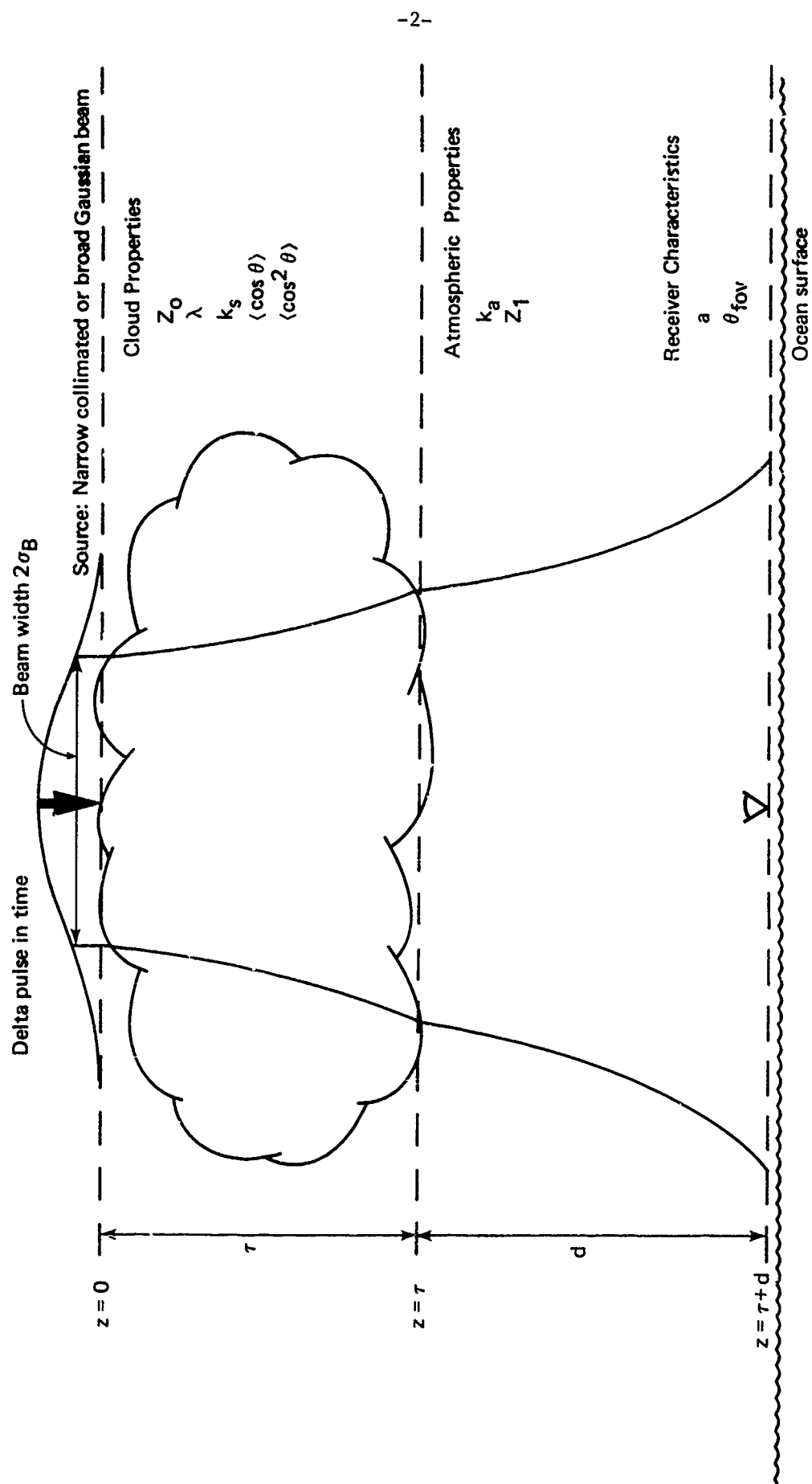


Fig. 1--Propagation path with model parameters

The most complete mathematical description of the multiple scattering problem is given by the nonstationary radiative transport equation of Chandrasekhar [2]. Written in dimensionless variables, the transport equation for the radiance $I(\underline{x}, \alpha; \xi)$ takes the form

$$\frac{\partial I(\underline{x}, \alpha; \xi)}{\partial \xi} + \underline{e}_\alpha \cdot \nabla_{\underline{x}} I = -I + \frac{\lambda}{4\pi} \int_{4\pi} I(\underline{x}, \alpha'; \xi) p(\alpha'; \alpha) d\omega_{\alpha'},$$

$$+ S_0(\underline{x}, \alpha; \xi), \quad (1)$$

where $\xi = k_e c t$ signifying time and k_e the extinction coefficient; $\underline{x} = k_e \underline{X}$ is the normalized cartesian spatial coordinate; $\alpha = (\theta, \phi)$ denotes an ordered pair of angular direction; and \underline{e}_α is the unit vector, and $d\omega_\alpha$ the solid-angle element, in direction α . In addition, $p(\alpha'; \alpha)$ is the scalar phase function, S_0 is the source function, and λ is the single-scatter albedo.

Unfortunately, the nonstationary transport equation has not been solved in a form suitable for computation. Hence two procedures have been widely used to obtain quantitative results--solving (1) under the small-angle assumption [3], and simulating the scattering process by computerized Monte Carlo methods [4].

Although the scalar phase function is indeed highly peaked in the forward direction for aerosols whose mean radius is much larger than the optical wavelength, the small-angle assumption may be invalid for clouds thicker than several mean free paths. In principle, Monte Carlo simulations can provide the required numerical results for studies of optical communication systems. In practice, however, the cost of simulations usually limits calculations to highly aggregated quantities (e.g., optical pulses collected over infinite receiving planes [4]). More important, Monte Carlo curve fits usually do not illuminate the underlying physical phenomena of interest.

To overcome such difficulties, we begin by deriving the first two spatial and angular moments of the radiance function for a narrow, collimated, delta-function source immersed in an infinite medium (Sec. II). The moments are expressed as simple closed-form algebraic formulae

derived with no approximations (e.g., small-angle assumption, restricted scalar phase function) and span the regimes from forward scatter (optically thin media) to diffusion (optically thick media). Their asymptotic limits are shown to correspond to the usual thin and thick cloud approximations (Sec. III).

In addition to clarifying the scattering process, the moments also provide the nonstationary drift and diffusion coefficients for the diffusion equation approximation to the transport equation (1). The full radiance distribution at the cloud exit (for $\tau \geq 15$) is derived from the energy density solution to the diffusion equation for finite cloud boundary conditions coupled with the published angular distribution for a diffusing particle emerging from a scattering medium (Sec. IV). The Green's function atmospheric propagator then allows power pulse calculations for a finite receiver placed an arbitrary distance below the cloud (Sec. V). Finally, the effect on the blue-green laser communication program is discussed (Sec. VI).

We validate the diffusion approximation to the transport process by comparing our calculations with published simulation curve fits for the functional form of received power versus time, total transmission versus the optical thickness of the cloud, spatial and angular spreading versus optical thickness, and multipath time delay versus optical thickness. In each case, the two methods show excellent agreement: the calculated curve generally overlaps the simulation fit for $\tau \geq 15$.

II. MOMENTS OF RADIANCE DISTRIBUTION

Consider a photon immersed in an infinite, nonabsorbing, scattering medium with collision geometry shown in Fig. 2. Path lengths between scatterings ℓ_n are independent, identically distributed (i.i.d.) random variables. The ℓ_n are distributed exponentially with a parameter of unity corresponding to randomly (i.e., Poisson) distributed aerosols and normalization of $\underline{x} = (x, y, z)^T$ to the mean scattering distance k_s^{-1} . Polar and rotational deflection angles-- θ_n and ϕ_n , respectively--are i.i.d. and distributed according to the scalar phase function, which is assumed to be such that θ_n and ϕ_n are independent and (by symmetry) ϕ_n is uniformly distributed on $(0, 2\pi)$.

The density function $f(\underline{x}, \alpha; \xi)$ is defined so that $f dV_{\underline{x}} d\omega_{\alpha}$ gives the probability that a photon initially heading in the z direction at $\underline{x} = 0$ will, at time $\xi = k_s ct$, be found in the volume element $dV_{\underline{x}} = dx dy dz$ while heading within the solid-angle element $d\omega_{\alpha}$ oriented in direction $\alpha = (\theta, \phi)$. The radiance $I(\underline{x}, \alpha; \xi)$ in dimensionless variables resulting from an initial, arbitrarily thin pulse in space and time is then given by $I(\underline{x}, \alpha; \xi) = E_0 f(\underline{x}, \alpha; \xi)$, where E_0 is the energy in the initial pulse.

Without explicit knowledge of $f(\underline{x}, \alpha; \xi)$, this section derives expressions for the following moments of the scattering process, all conditioned on a photon initially at $\underline{x} = 0$ and directed along the z -axis in an infinite nonabsorbing medium.

- The mean penetration into the medium at time ξ :

$$\bar{z}(\xi) = \int_{V_x} \int_{\Omega} z f dV_{\underline{x}} d\omega_{\alpha} .$$

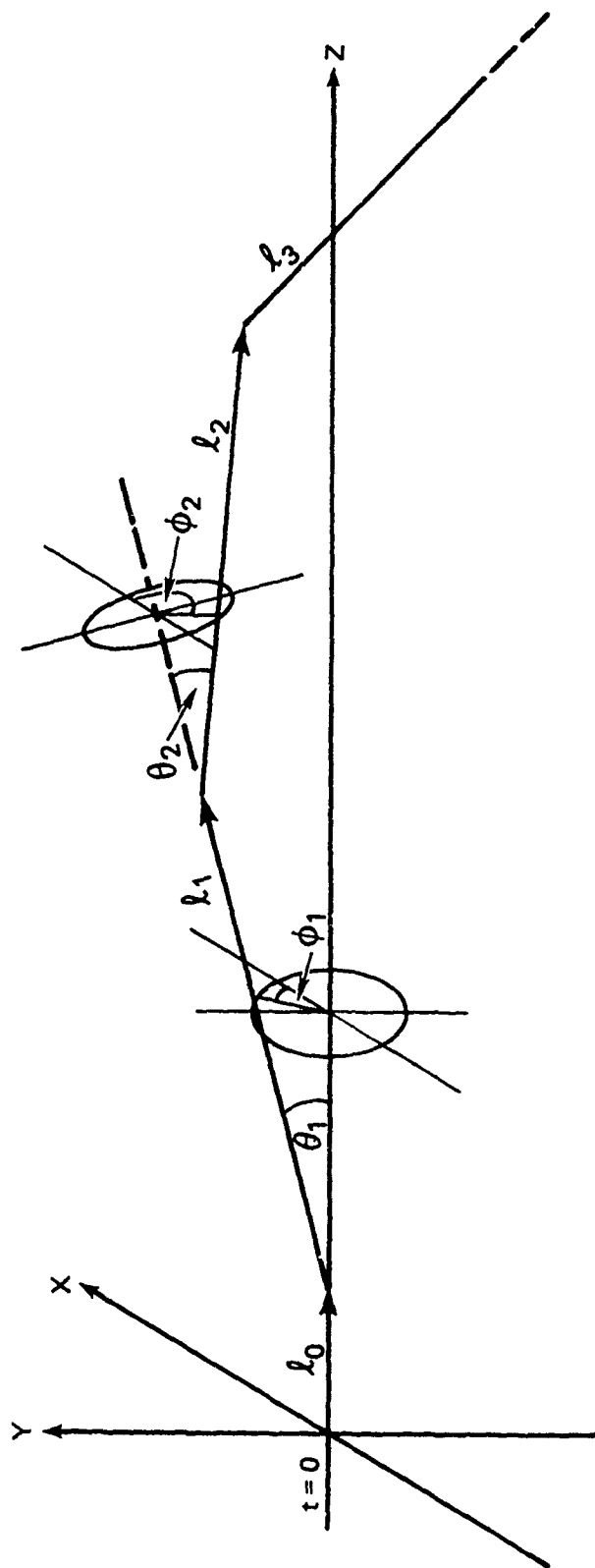


Fig. 2--Scattering geometry

- The variance along the axis of propagation:

$$\sigma_z^2(\xi) = \int_{V_{\underline{x}}} \int_{\Omega} [z - \bar{z}(\xi)]^2 f \, dV_{\underline{x}} \, d\omega_{\alpha} .$$

- The transverse variance:

$$\sigma_x^2(\xi) = \sigma_y^2(\xi) = \int_{V_{\underline{x}}} \int_{\Omega} x^2 f \, dV_{\underline{x}} \, d\omega_{\alpha} .$$

- The average cosine of the polar heading at time ξ :

$$\langle \cos \theta(\xi) \rangle = \int_{V_{\underline{x}}} \int_{\Omega} \cos \theta \, f \, dV_{\underline{x}} \, d\omega_{\alpha} .$$

- The mean of $\cos^2 \theta(\xi)$:

$$\langle \cos^2 \theta(\xi) \rangle = \int_{V_{\underline{x}}} \int_{\Omega} \cos^2 \theta \, f \, dV_{\underline{x}} \, d\omega_{\alpha} ,$$

where the solid-angle integrals are over $\Omega = 4\pi$ steradians and $\bar{x}(\xi) = \bar{y}(\xi) \equiv 0$ by symmetry.

The following derivations are included for mathematical completeness, and may be omitted by those most interested in the physical significance of the moments described in Sec. III.

The derivations proceed in two parts. First, the (conditional) moments of $f_n(\underline{x}, \alpha; \xi)$ --i.e., the volume-angle density restricted to photons that have scattered exactly n times--are found; then the unconditional moments are computed directly as, for example,

$$\bar{z}(\xi) = \sum_{n=0}^{\infty} \mathcal{P}\{n(\xi) = n\} \bar{z}_n(\xi) ,$$

where the probability of n scatterings at time $\xi \geq 0$ is given by

$$\mathcal{P}\{n(\xi) = n\} = \frac{\xi^n}{n!} e^{-\xi} , \quad n \geq 0 . \quad (2)$$

CONDITIONAL MEAN $\bar{x}_n(\xi)$

At time ξ the random position vector of a photon initially at $\underline{x} = 0$ traveling in z direction and scattered n times is

$$\begin{pmatrix} x_n(\xi) \\ y_n(\xi) \\ z_n(\xi) \end{pmatrix} = \underline{x}_n(\xi) = \sum_{m=0}^n \ell_m(\xi) \underline{v}_m , \quad (3)$$

where

$$\underline{v}_m = \prod_{k=0}^m B_k \begin{pmatrix} 0 \\ 0 \\ 1 \end{pmatrix} , \quad (4)$$

ℓ_m is the random distance traveled by the photon between the m and $m+1$ scattering, and B_k is a matrix giving the *change* in heading after the k^{th} scattering event. Therefore,

$$B_0 = \begin{pmatrix} 1 & 0 & 0 \\ 0 & 1 & 0 \\ 0 & 0 & 1 \end{pmatrix}$$

and

$$B_k = \begin{pmatrix} \cos \phi_k \cos \theta_k & -\sin \phi_k & \cos \phi_k \sin \theta_k \\ \sin \phi_k \cos \theta_k & \cos \phi_k & \sin \phi_k \sin \theta_k \\ -\sin \theta_k & 0 & \cos \theta_k \end{pmatrix} .$$

The independence of the θ_k and ϕ_k imply the independence of the B_k , although ℓ_m is not independent of $\ell_{m'}$, for all $m, m' \leq n$, when conditioned on a total of n scatterings.

Taking the expectation of Eq. (3), we have

$$\bar{x}_n(\xi) = \sum_{m=0}^n \bar{\ell}_m \bar{v}_m. \quad (3')$$

To evaluate $\bar{\ell}_m$, we must digress into order statistics. Given that the photon has been scattered n times at time ξ , let $\tau_1, \tau_2, \dots, \tau_n$ be the ordered random scattering times. Since unordered scattering times are i.i.d. and uniform on $[0, \xi]$, the ordered random scattering times have the joint probability density [5]

$$f_{\tau_1, \tau_2, \dots, \tau_n}(\xi_1, \xi_2, \dots, \xi_n) = \frac{n!}{\xi^n}, \quad 0 \leq \xi_1 \leq \xi_2 \leq \dots \leq \xi_n \leq \xi$$

$$= 0, \quad \text{otherwise.}$$

The scattering lengths are related to the order statistics by the formula

$$\ell_k = \tau_{k+1} - \tau_k, \quad k = 0, 1, \dots, n. \quad (5)$$

Thus,

$$\bar{\tau}_k = \frac{n!}{\xi^n} \left(\int_0^\xi d\xi_n \int_0^{\xi_n} d\xi_{n-1} \dots \int_0^{\xi_{k+2}} d\xi_{k+1} \int_0^{\xi_{k+1}} d\xi_k \xi_k \right.$$

$$\left. \times \int_0^{\xi_k} d\xi_{k-1} \dots \int_0^{\xi_3} d\xi_2 \int_0^{\xi_2} d\xi_1 \right) = \frac{k\xi}{n+1}$$

and

$$\bar{\ell}_m = \langle \tau_{m+1} - \tau_m \rangle = \bar{\tau}_{m+1} - \bar{\tau}_m = \frac{\xi}{n+1}.$$

Since the B_k are i.i.d, it follows from Eq. (4) that

$$\bar{v}_m = \bar{B}_0 \bar{B}_1 \bar{B}_2 \cdots \bar{B}_m \begin{pmatrix} 0 \\ 0 \\ 1 \end{pmatrix} = \bar{B}^m \begin{pmatrix} 0 \\ 0 \\ 1 \end{pmatrix},$$

where

$$\bar{B} = \begin{pmatrix} 0 & 0 & 0 \\ 0 & 0 & 0 \\ -\langle \sin \theta \rangle & 0 & \langle \cos \theta \rangle \end{pmatrix}. \quad (6)$$

Thus,

$$\bar{v}_m = \begin{pmatrix} 0 \\ 0 \\ \langle \cos \theta \rangle^m \end{pmatrix}.$$

Letting $v = 1 - g = 1 - \langle \cos \theta \rangle$, with the help of Eq. (3') we finally obtain

$$\bar{x}_n(\xi) = \bar{y}_n(\xi) \equiv 0 \quad (7)$$

and

$$\bar{z}_n(\xi) = \frac{\xi}{n+1} \frac{1 - (1-v)^{n+1}}{v}. \quad (8)$$

CONDITIONAL SECOND MOMENT $\langle \underline{x}_n(\xi) \underline{x}_n^T(\xi) \rangle$

Multiplying the random position vector in Eq. (3) by its transpose gives

$$\begin{aligned} \underline{x}_n(\xi) \underline{x}_n^T(\xi) &= \left(\sum_{m=0}^n \ell_m(\xi) \underline{v}_m \right) \left(\sum_{k=0}^n \ell_k(\xi) \underline{v}_k \right)^T \\ &= \sum_{m=0}^n \sum_{k=0}^n \ell_m(\xi) \ell_k(\xi) \underline{v}_m \underline{v}_k^T. \end{aligned}$$

Taking expectations and using the independence of the ℓ_m and \underline{v}_m yields

$$\begin{aligned} \langle \underline{x}_n(\xi) \underline{x}_n^T(\xi) \rangle &= \sum_{m=0}^n \sum_{k=0}^n \langle \ell_m \ell_k \rangle \langle \underline{v}_m \underline{v}_k^T \rangle \\ &= \sum_{m=0}^n \langle \ell_m^2 \rangle \langle \underline{v}_m \underline{v}_m^T \rangle + 2 \sum_{m=1}^n \sum_{k=0}^{m-1} \langle \ell_m \ell_k \rangle \langle \underline{v}_m \underline{v}_k^T \rangle. \quad (9) \end{aligned}$$

From Eq. (5) we have

$$\ell_m^2 = (\tau_{m+1} - \tau_m)^2$$

and

$$\ell_m \ell_k = (\tau_{m+1} - \tau_m)(\tau_{k+1} - \tau_k).$$

Now,

$$\begin{aligned} \langle \tau_k^2 \rangle &= \frac{n!}{\xi^n} \left(\int_0^\xi d\xi_n \int_0^{\xi_n} d\xi_{n-1} \cdots \int_0^{\xi_{k+2}} d\xi_{k+1} \int_0^{\xi_{k+1}} d\xi_k \xi_k^2 \right. \\ &\quad \left. \times \int_0^{\xi_k} d\xi_{k-1} \cdots \int_0^{\xi_3} d\xi_2 \int_0^{\xi_2} d\xi_1 \right) = \frac{k(k+1)\xi^2}{(n+1)(n+2)} \end{aligned}$$

and

$$\begin{aligned} \langle \tau_j \tau_k \rangle &= \frac{n!}{\xi^n} \left(\int_0^\xi d\xi_n \int_0^{\xi_n} d\xi_{n-1} \cdots \int_0^{\xi_{k+2}} d\xi_{k+1} \int_0^{\xi_{k+1}} d\xi_k \xi_k \right. \\ &\quad \times \int_0^{\xi_k} d\xi_{k-1} \cdots \int_0^{\xi_{j+2}} d\xi_{j+1} \int_0^{\xi_{j+1}} d\xi_j \xi_j \\ &\quad \left. \times \int_0^{\xi_j} d\xi_{j-1} \cdots \int_0^{\xi_3} d\xi_2 \int_0^{\xi_2} d\xi_1 \right) = \frac{j(k+1)\xi^2}{(n+1)(n+2)}, \end{aligned}$$

for $k > j$,

so that

$$\langle \tau_j \tau_k \rangle = \frac{j(k+1)\xi^2}{(n+1)(n+2)}, \quad \text{for } k \geq j.$$

Thus,

$$\langle \ell_m^2 \rangle = \langle (\tau_{m+1} - \tau_m)^2 \rangle = \langle \tau_{m+1}^2 \rangle - 2\langle \tau_m \tau_{m+1} \rangle + \langle \tau_m^2 \rangle = \frac{2\xi^2}{(n+1)(n+2)}$$

and

$$\begin{aligned} \langle \ell_m \ell_k \rangle &= \langle (\tau_{m+1} - \tau_m)(\tau_{k+1} - \tau_k) \rangle \\ &= \langle \tau_{m+1} \tau_{k+1} \rangle - \langle \tau_{m+1} \tau_k \rangle - \langle \tau_m \tau_{k+1} \rangle + \langle \tau_m \tau_k \rangle \\ &= \frac{\xi^2}{(n+1)(n+2)} = 2\langle \ell_m^2 \rangle, \quad \text{for } m > k. \end{aligned}$$

Substituting the above results into Eq. (9) and separating the zeroth term in the first summation, we obtain

$$\begin{aligned} \langle \underline{x}_n(\xi) \underline{x}_n^T(\xi) \rangle = & \frac{2\xi^2}{(n+1)(n+2)} \left[\begin{pmatrix} 0 & 0 & 0 \\ 0 & 0 & 0 \\ 0 & 0 & 1 \end{pmatrix} + \sum_{m=1}^n \langle \underline{v}_m \underline{v}_m^T \rangle \right. \\ & \left. + \sum_{m=1}^n \sum_{k=0}^{m-1} \langle \underline{v}_m \underline{v}_k^T \rangle \right]. \end{aligned} \quad (10)$$

From Eqs. (4) and (6), we have

$$\begin{aligned} \langle \underline{v}_m \underline{v}_k^T \rangle &= \langle B_1 \cdots B_k B_{k+1} B_{k+2} \cdots B_m \begin{pmatrix} 0 \\ 0 \\ 1 \end{pmatrix} \underline{v}_k^T \rangle \\ &= \langle B_1 \cdots B_k \langle B_{k+1} B_{k+2} \cdots B_m \rangle \begin{pmatrix} 0 \\ 0 \\ 1 \end{pmatrix} \underline{v}_k^T \rangle \\ &= \langle B_1 \cdots B_k \overline{B}^{m-k} \begin{pmatrix} 0 \\ 0 \\ 1 \end{pmatrix} \underline{v}_k^T \rangle \\ &= \langle B_1 \cdots B_k \langle \cos \theta \rangle^{m-k} \begin{pmatrix} 0 \\ 0 \\ 1 \end{pmatrix} \underline{v}_k^T \rangle \\ &= \langle \cos \theta \rangle^{m-k} \langle \underline{v}_k \underline{v}_k^T \rangle \\ &= g^{m-k} \langle \underline{v}_k \underline{v}_k^T \rangle. \end{aligned} \quad (11)$$

Substituting Eq. (11) into Eq. (10) and separating terms with $k = 0$ in the double sum of Eq. (10), we obtain

$$\begin{aligned}
 \langle \underline{x}_n(\xi) \underline{x}_n^T(\xi) \rangle &= \frac{2\xi^2}{(n+1)(n+2)} \left[\begin{pmatrix} 0 & 0 & 0 \\ 0 & 0 & 0 \\ 0 & 0 & 1 \end{pmatrix} + \sum_{m=1}^n \langle \underline{v}_m \underline{v}_m^T \rangle \right. \\
 &\quad \left. + \sum_{m=1}^n g^m \begin{pmatrix} 0 & 0 & 0 \\ 0 & 0 & 0 \\ 0 & 0 & 1 \end{pmatrix} + \sum_{m=2}^n \sum_{k=1}^{m-1} g^{m-k} \langle \underline{v}_k \underline{v}_k^T \rangle \right] \\
 &= \frac{2\xi^2}{(n+1)(n+2)} \left[\frac{1-g^{n+1}}{1-g} \begin{pmatrix} 0 & 0 & 0 \\ 0 & 0 & 0 \\ 0 & 0 & 1 \end{pmatrix} + \sum_{m=1}^n \langle \underline{v}_m \underline{v}_m^T \rangle \right. \\
 &\quad \left. + \sum_{k=1}^{n-1} \langle \underline{v}_k \underline{v}_k^T \rangle \left(\sum_{m=1}^{n-k} g^m \right) \right] \\
 &= \frac{2\xi^2}{(n+1)(n+2)} \left[\frac{1-g^{n+1}}{1-g} \begin{pmatrix} 0 & 0 & 0 \\ 0 & 0 & 0 \\ 0 & 0 & 1 \end{pmatrix} + \sum_{m=1}^n \langle \underline{v}_m \underline{v}_m^T \rangle \right. \\
 &\quad \left. + \frac{g}{1-g} \sum_{k=1}^{n-1} \langle \underline{v}_k \underline{v}_k^T \rangle - \frac{g^{n+1}}{1-g} \sum_{k=1}^{n-1} g^{-k} \langle \underline{v}_k \underline{v}_k^T \rangle \right].
 \end{aligned}
 \tag{12}$$

The evaluation of $\langle \underline{v}_k \underline{v}_k^T \rangle$ proceeds by taking expectations from the center outward:

$$\begin{aligned}
 \langle \underline{v}_k \underline{v}_k^T \rangle &= \langle B_1 B_2 \cdots B_{k-1} B_k \begin{pmatrix} 0 & 0 & 0 \\ 0 & 0 & 0 \\ 0 & 0 & 1 \end{pmatrix} B_k^T B_{k-1}^T \cdots B_2^T B_1^T \rangle \\
 &= \langle B_1 \rangle \langle B_2 \rangle \cdots \langle B_{k-1} \rangle \langle B_k \begin{pmatrix} 0 & 0 & 0 \\ 0 & 0 & 0 \\ 0 & 0 & 1 \end{pmatrix} B_k^T \rangle \cdots B_2^T B_1^T \\
 &= \langle B_1 \rangle \langle B_2 \rangle \cdots \langle B_{k-1} \rangle \begin{pmatrix} \frac{1}{2} \langle \sin^2 \theta \rangle & 0 & 0 \\ 0 & \frac{1}{2} \langle \sin^2 \theta \rangle & 0 \\ 0 & 0 & \langle \cos^2 \theta \rangle \end{pmatrix} B_{k-1}^T \cdots B_2^T B_1^T \\
 &\quad \vdots \\
 &= \frac{1}{3} \begin{pmatrix} 1 - \zeta^k & 0 & 0 \\ 0 & 1 - \zeta^k & 0 \\ 0 & 0 & 1 + 2\zeta^k \end{pmatrix}, \tag{13}
 \end{aligned}$$

where

$$\zeta = \frac{3 \langle \cos^2 \theta \rangle - 1}{2}.$$

Since

$$\sum_{m=1}^n \zeta^m = \frac{\zeta(1 - \zeta^n)}{1 - \zeta},$$

Eq. (12) becomes

$$\begin{aligned}
 \langle \underline{x}_n(\xi) \underline{x}_n^T(\xi) \rangle &= \frac{2\xi^2}{(n+1)(n+2)} \left\{ \frac{1-g^{n+1}}{1-g} \begin{pmatrix} 0 & 0 & 0 \\ 0 & 0 & 0 \\ 0 & 0 & 1 \end{pmatrix} + \frac{n}{3} \begin{pmatrix} 1 & 0 & 0 \\ 0 & 1 & 0 \\ 0 & 0 & 1 \end{pmatrix} \right. \\
 &\quad + \frac{1}{3} \frac{\zeta(1-\zeta^n)}{1-\zeta} \begin{pmatrix} -1 & 0 & 0 \\ 0 & -1 & 0 \\ 0 & 0 & 2 \end{pmatrix} + \frac{n-1}{3} \frac{g}{1-g} \begin{pmatrix} 1 & 0 & 0 \\ 0 & 1 & 0 \\ 0 & 0 & 1 \end{pmatrix} \\
 &\quad + \frac{1}{3} \frac{g}{1-g} \frac{\zeta(1-\zeta^{n-1})}{1-\zeta} \begin{pmatrix} -1 & 0 & 0 \\ 0 & -1 & 0 \\ 0 & 0 & 2 \end{pmatrix} - \frac{1}{3} \frac{g}{1-g} \frac{g(1-g^{n-1})}{1-g} \begin{pmatrix} 1 & 0 & 0 \\ 0 & 1 & 0 \\ 0 & 0 & 1 \end{pmatrix} \\
 &\quad \left. - \frac{1}{3} \frac{g^{n+1}}{1-g} \frac{(\zeta/g)[1-(\zeta/g)^{n-1}]}{1-\zeta/g} \begin{pmatrix} -1 & 0 & 0 \\ 0 & -1 & 0 \\ 0 & 0 & 2 \end{pmatrix} \right\} \\
 &= \frac{2\xi^2}{2(n+1)(n+2)} \left\{ 3 \begin{pmatrix} 0 & 0 & 0 \\ 0 & 0 & 0 \\ 0 & 0 & 1 \end{pmatrix} \left(\frac{1-g^{n+1}}{1-g} \right) + \begin{pmatrix} 1 & 0 & 0 \\ 0 & 1 & 0 \\ 0 & 0 & 1 \end{pmatrix} \left[\frac{n}{1-g} - \frac{g(1-g^n)}{(1-g)^2} \right] \right. \\
 &\quad \left. + \begin{pmatrix} -1 & 0 & 0 \\ 0 & -1 & 0 \\ 0 & 0 & 2 \end{pmatrix} \left[\frac{\zeta(1-\zeta^n)}{1-\zeta} + \frac{g\zeta(1-\zeta^{n-1})}{(1-g)(1-\zeta)} - \frac{g^2\zeta(g^{n-1}-\zeta^{n-1})}{(1-g)(g-\zeta)} \right] \right\}.
 \end{aligned}
 \tag{14}$$

But

$$\langle \underline{x}_n(\xi) \underline{x}_n^T(\xi) \rangle = \begin{pmatrix} \langle x_n^2(\xi) \rangle & \langle x_n(\xi) y_n(\xi) \rangle & \langle x_n(\xi) z_n(\xi) \rangle \\ \langle y_n(\xi) x_n(\xi) \rangle & \langle y_n^2(\xi) \rangle & \langle y_n(\xi) z_n(\xi) \rangle \\ \langle z_n(\xi) x_n(\xi) \rangle & \langle z_n(\xi) y_n(\xi) \rangle & \langle z_n^2(\xi) \rangle \end{pmatrix}.$$

Thus, after combining terms in Eq. (14), we conclude that

$$\langle x_n^2(\xi) \rangle = \langle y_n^2(\xi) \rangle = \frac{2\xi^2}{3(n+1)(n+2)} \times \left\{ \frac{w^2[(1-v)^{n+2} - 1 + (n+2)v] - v^2[(1-w)^{n+2} - 1 + (n+2)w]}{wv(w-v)} \right\} \quad (15)$$

and

$$\langle z_n^2(\xi) \rangle = \frac{2\xi^2}{3(n+1)(n+2)} \times \left\{ \frac{(w^2 - 3wv)[(1-v)^{n+2} - 1 + (n+2)v] + 2v^2[(1-w)^{n+2} - 1 + (n+2)w]}{wv^2(w-v)} \right\}, \quad (16)$$

where

$$v = 1 - g = 1 - \langle \cos \theta \rangle$$

and

$$w = 1 - \zeta = \frac{3}{2} (1 - \langle \cos^2 \theta \rangle).$$

CONDITIONAL ANGULAR MOMENTS $\langle \cos \theta \rangle_n$ and $\langle \cos^2 \theta \rangle_n$

Let B_H be the rotation matrix resulting from n scatterings, so that

$$B_H = B_0 B_1 \cdots B_n.$$

Taking expectations and using Eq. (6), we obtain

$$\bar{B}_H = \bar{B}^n = \begin{pmatrix} 0 & 0 & 0 \\ 0 & 0 & 0 \\ -\langle \sin \theta \rangle \langle \cos \theta \rangle^{n-1} & 0 & \langle \cos \theta \rangle^n \end{pmatrix}.$$

But by definition

$$\bar{B}_H = \begin{pmatrix} 0 & 0 & 0 \\ 0 & 0 & 0 \\ -\langle \sin \theta \rangle_n & 0 & \langle \cos \theta \rangle_n \end{pmatrix}.$$

Matching entries in the last two expressions for \bar{B}_H , the expectation of the polar angle cosine after n scatterings is given by

$$\langle \cos \theta \rangle_n = \langle \cos \theta \rangle^n = g^n = (1 - v)^n. \quad (17)$$

Similarly,

$$\begin{aligned} \langle \underline{v}_n \underline{v}_n^T \rangle &= \langle B_H \begin{pmatrix} 0 & 0 & 0 \\ 0 & 0 & 0 \\ 0 & 0 & 1 \end{pmatrix} B_H^T \rangle \\ &= \begin{pmatrix} 1/2 \langle \sin^2 \theta \rangle_n & 0 & 0 \\ 0 & 1/2 \langle \sin^2 \theta \rangle_n & 0 \\ 0 & 0 & \langle \cos^2 \theta \rangle_n \end{pmatrix}, \end{aligned}$$

so, after matching terms with Eq. (13),

$$\langle \cos^2 \theta \rangle_n = \frac{1}{3} (1 + 2v^n) = \frac{1}{3} [1 + 2(1 - w)^n]. \quad (18)$$

UNCONDITIONAL MOMENTS

We calculate the unconditional moments from the conditional moments after observing that the probability of a photon undergoing exactly n scatterings at time ξ is Poisson-distributed with mean ξ , as in Eq. (2). Hence from Eqs. (7) and (8), we obtain

$$\bar{x}(\xi) = \sum_{n=0}^{\infty} \mathcal{P}\{n(\xi) = n\} \bar{x}_n(\xi) = 0, \quad (19)$$

$$\bar{y}(\xi) = \sum_{n=0}^{\infty} \mathcal{P}\{n(\xi) = n\} \bar{y}_n(\xi) = 0, \quad (20)$$

and

$$\begin{aligned} \bar{z}(\xi) &= \sum_{n=0}^{\infty} \mathcal{P}\{n(\xi) = n\} \bar{z}_n(\xi) \\ &= \sum_{n=0}^{\infty} \frac{e^{-\xi} \xi^n}{n!} \frac{\xi}{n+1} \frac{1 - (1-v)^{n+1}}{v} \\ &= \frac{e^{-\xi}}{v} \left\{ \sum_{n=0}^{\infty} \frac{\xi^{n+1}}{(n+1)!} - \sum_{n=0}^{\infty} \frac{[\xi(1-v)]^{n+1}}{(n+1)!} \right\} \\ &= \frac{e^{-\xi}}{v} \left[e^{\xi} - 1 - (e^{\xi(1-v)} - 1) \right] \\ &= \frac{1 - e^{-v\xi}}{v}. \end{aligned} \quad (21)$$

Similarly, to calculate the unconditional spatial variance $\sigma_x^2(\xi)$, we combine Eqs. (2), (15), and (19) to obtain

$$\sigma_x^2(\xi) = \langle x^2(\xi) \rangle - \bar{x}^2(\xi)$$

$$= \sum_{n=0}^{\infty} \mathcal{P}\{n(\xi) = n\} \langle x_n^2(\xi) \rangle$$

$$= \sum_{n=0}^{\infty} \frac{e^{-\xi} \xi^n}{n!} \frac{2\xi^2}{3(n+1)(n+2)}$$

$$\times \left\{ \frac{w^2[(1-v)^{n+2} - 1 + (n+2)v] - v^2[(1-w)^{n+2} - 1 + (n+2)w]}{wv^2(w-v)} \right\}$$

$$= \frac{2e^{-\xi}}{3wv^2(w-v)} \left[w^2 \left\{ \sum_{n=0}^{\infty} \frac{[(1-v)\xi]^{n+2}}{(n+2)!} \right. \right.$$

$$\left. - \sum_{n=0}^{\infty} \frac{\xi^{n+2}}{(n+2)!} + v\xi \sum_{n=0}^{\infty} \frac{\xi^{n+1}}{(n+1)!} \right\}$$

$$\left. - v^2 \left\{ \sum_{n=0}^{\infty} \frac{[(1-w)\xi]^{n+2}}{(n+2)!} - \sum_{n=0}^{\infty} \frac{\xi^{n+2}}{(n+2)!} + w\xi \sum_{n=0}^{\infty} \frac{\xi^{n+1}}{(n+1)!} \right\} \right].$$

Since

$$\sum_{n=0}^{\infty} \frac{\xi^{n+1}}{(n+1)!} = e^{\xi} - 1$$

and

$$\sum_{n=0}^{\infty} \frac{\xi^{n+2}}{(n+2)!} = e^{\xi} - 1 - \xi,$$

combining terms yields

$$\sigma_x^2(\xi) = \frac{2}{3} \frac{w^2(e^{-v\xi} - 1 + v\xi) - v^2(e^{-w\xi} - 1 + w\xi)}{wv^2(w - v)}. \quad (22)$$

From Eq. (15), $\langle y^2(\xi) \rangle = \langle x^2(\xi) \rangle$; therefore,

$$\sigma_y^2(\xi) = \frac{2}{3} \frac{w^2(e^{-v\xi} - 1 + v\xi) - v^2(e^{-w\xi} - 1 + w\xi)}{wv^2(w - v)}. \quad (23)$$

Likewise, to compute $\sigma_z^2(\xi)$ we use Eqs. (2) and (16) to obtain

$$\begin{aligned} \langle z^2(\xi) \rangle &= \sum_{n=0}^{\infty} \mathcal{P}\{n(\xi) = n\} \langle z_n^2(\xi) \rangle \\ &= \sum_{n=0}^{\infty} \frac{e^{-\xi} \xi^n}{n!} \frac{2\xi^2}{3(n+1)(n+2)} \\ &\quad \times \left\{ \frac{(w^2 - 3wv)[(1-v)^{n+2} - 1 + (n+2)v] + 2v^2[(1-w)^{n+2} - 1 + (n+2)w]}{wv^2(w-v)} \right\} \\ &= \frac{2}{3} \frac{(w^2 - 3wv)(e^{-v\xi} - 1 + v\xi) + 2v^2(e^{-w\xi} - 1 + w\xi)}{wv^2(w-v)}. \end{aligned}$$

Thus,

$$\begin{aligned} \sigma_z^2(\xi) &= \langle z^2(\xi) \rangle - \bar{z}^2(\xi) \\ &= \frac{2}{3} \frac{(w^2 - 3wv)(e^{-v\xi} - 1 + v\xi) + 2v^2(e^{-w\xi} - 1 + w\xi)}{wv^2(w-v)} \\ &\quad - \left(\frac{1 - e^{-v\xi}}{v} \right)^2. \end{aligned} \quad (24)$$

The calculation of the unconditional angular moments proceeds in the same manner. Thus, Eqs. (12) and (17) yield

$$\begin{aligned}
 \langle \cos \theta(\xi) \rangle &= \sum_{n=0}^{\infty} \mathcal{P}\{n(\xi) = n\} \langle \cos \theta \rangle_n \\
 &= \sum_{n=0}^{\infty} \frac{e^{-\xi} \xi^n}{n!} (1 - v)^n = e^{-\xi} e^{\xi(1-v)} \\
 &= e^{-v\xi},
 \end{aligned} \tag{25}$$

and Eqs. (2) and (18) yield

$$\begin{aligned}
 \langle \cos^2 \theta(\xi) \rangle &= \sum_{n=0}^{\infty} \mathcal{P}\{n(\xi) = n\} \langle \cos^2 \theta \rangle_n \\
 &= \sum_{n=0}^{\infty} \frac{e^{-\xi} \xi^n}{n!} \left\{ \frac{1}{3} [1 + 2(1 - w)^n] \right\} \\
 &= \frac{1}{3} e^{-\xi} \left\{ \sum_{n=0}^{\infty} \frac{\xi^n}{n!} + 2 \sum_{n=0}^{\infty} \frac{[(1 - w)\xi]^n}{n!} \right\} \\
 &= \frac{1}{3} e^{-\xi} \left(e^{\xi} + 2e^{\xi(1-w)} \right) \\
 &= \frac{1}{3} (1 + 2e^{-w\xi}).
 \end{aligned} \tag{26}$$

III. MOMENT ILLUSTRATIONS AND ASYMPTOTICS

Here we examine the physical significance of the moment formulae as well as their behavior for small and large times to allow comparison with published results and to demonstrate the transition between the diffusion and forward scatter regimes. Our discussion is predicated on the assumption of an arbitrarily thin, delta-function time pulse immersed in an infinite nonabsorbing medium. Section IV extends our results to a finite cloud with absorption, and Sec. V considers a broad Gaussian beam at the cloud entrance and an atmospheric layer below the cloud.

DIFFUSION REGIME

It is convenient to consider a simple diffusion (e.g., Brownian motion) as the limiting process obtained when a particle suffers an arbitrarily large number of isotropic scatterings separated by arbitrarily small path lengths. The moments of the particle distribution are then consistent with a stationary centroid at $\underline{x} = 0$, a spatial variance along each coordinate that grows linearly with time, and an isotropic heading independent of time. Although individual photon deflections within a cloud are highly anisotropic, after a photon undergoes many scatterings, its behavior may be expected to resemble that of a diffusing particle. This intuitive notion is verified by the moment formulae below.

Figures 3 and 4 illustrate the temporal behavior of the first two spatial moments of the scattering process. Figure 3 plots $\bar{z}(\xi)$ computed from Eq. (21) for several values of $\langle \cos \theta \rangle$. The asymptotic limit of $\bar{z}(\xi)$ is

$$\lim_{\xi \rightarrow \infty} \bar{z}(\xi) = \frac{1}{1 - \langle \cos \theta \rangle} . \quad (27)$$

The centroid of the photon density is thus stationary at about $z = 7$ for $\xi > 20$ when $\langle \cos \theta \rangle = 0.85$, a representative value for cloud aerosols [1]. Figure 4 plots $\sigma_x(\xi)$ and $\sigma_z(\xi)$ from Eqs. (22) and (24),

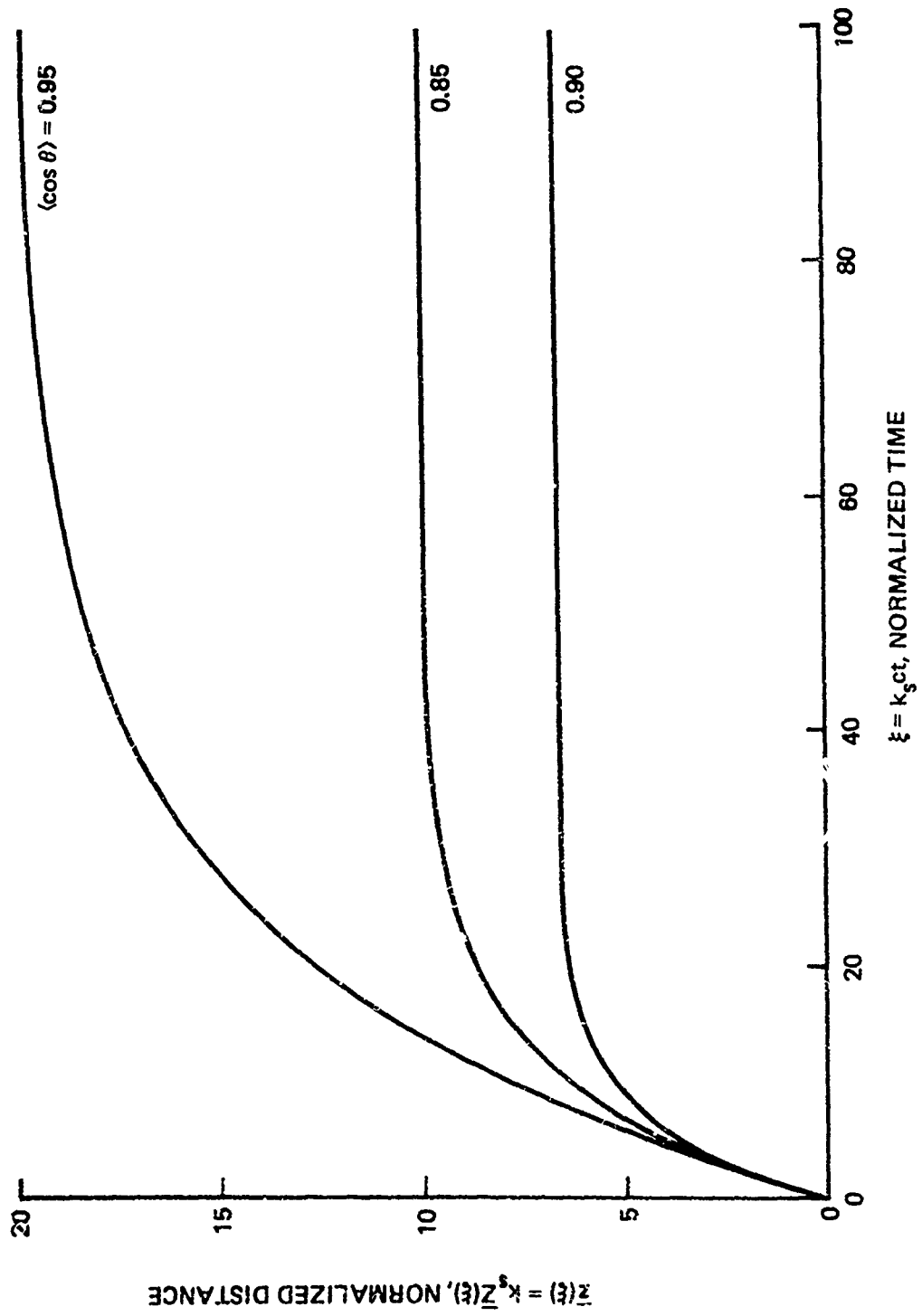


Fig. 3--Mean photon penetration parameterized on $\langle \cos \theta \rangle$

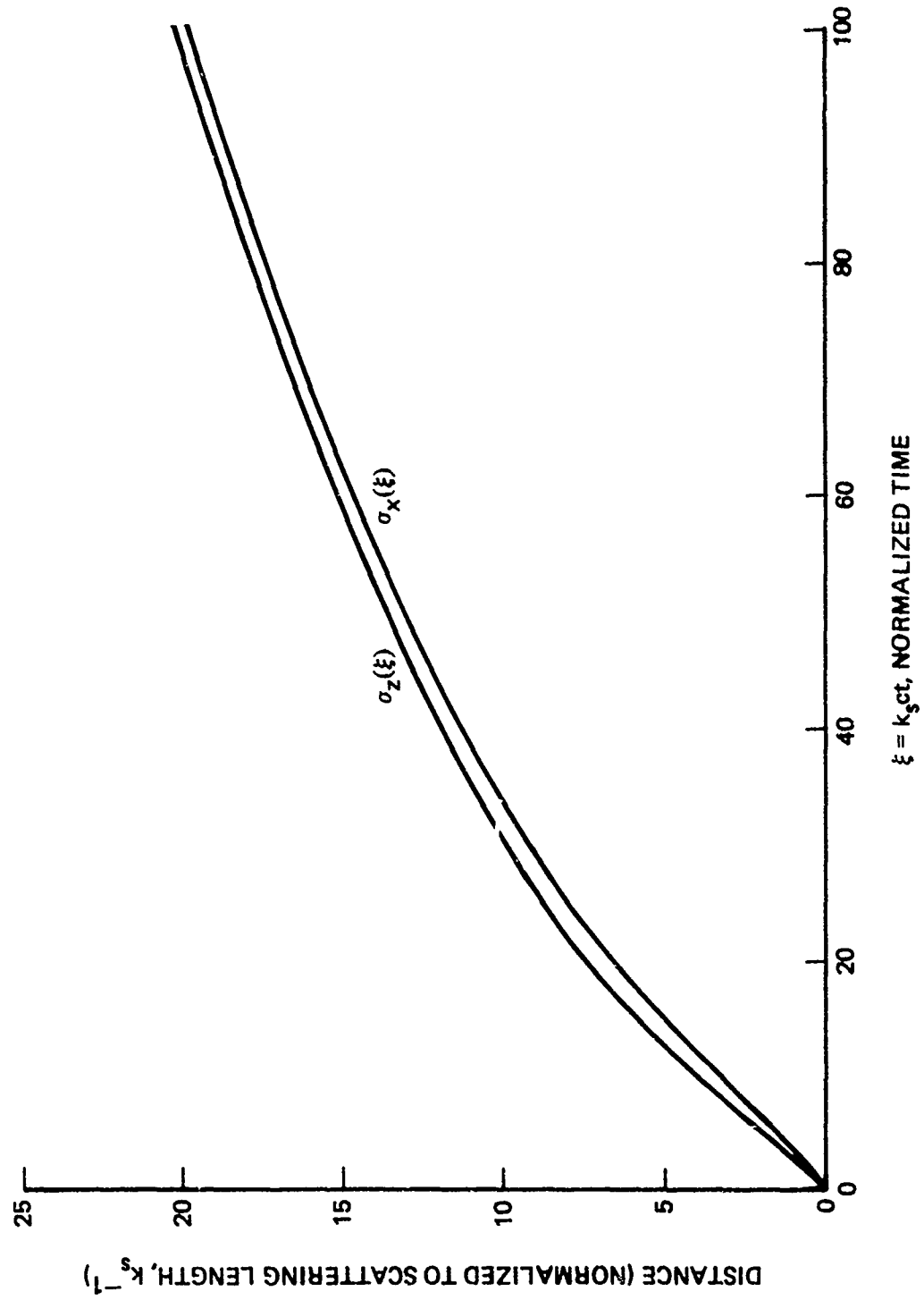


Fig. 4--Spatial standard deviations plotted for $\langle \cos \theta \rangle = \langle \cos^2 \theta \rangle = 0.850$

respectively, for $\langle \cos \theta \rangle = \langle \cos^2 \theta \rangle = 0.85$. The asymptotic limit of the corresponding variances is given by

$$\sigma_x^2(\xi) = \sigma_z^2(\xi) = \frac{2}{3} \frac{\xi}{1 - \langle \cos \theta \rangle} \quad (28)$$

for large ξ . Equation (28) evaluated for $\langle \cos \theta \rangle = 0$ (isotropic scattering) is the classical diffusion result for Brownian motion [6]. Equations (27) and (28) also evince the $1 - \langle \cos \theta \rangle$ factor suggested for scaling diffusion results [4].

To conclude that the photon distribution for large times resembles that of a diffusing particle, we must inspect the behavior of the angular as well as the spatial moments. From Eqs. (25) and (26) in Sec. II,

$$\langle \cos \theta(\xi) \rangle = e^{-v\xi} \quad (29)$$

and

$$\begin{aligned} \sigma_{\cos \theta}^2(\xi) &= \langle \cos^2 \theta(\xi) \rangle - \langle \cos \theta(\xi) \rangle^2 \\ &= \frac{1}{3} (1 + 2e^{-w\xi}) - e^{-2v\xi}, \end{aligned} \quad (30)$$

where $\theta(\xi)$ is the polar direction of the photon at normalized time ξ .

Figure 5 plots $\langle \cos \theta(\xi) \rangle$ and $\sigma_{\cos \theta}^2(\xi)$ for $\langle \cos \theta \rangle = \langle \cos^2 \theta \rangle = 0.85$. The asymptotic limit of $\langle \cos \theta(\xi) \rangle$ is zero, corresponding to a diffusion-like isotropic polar heading; and

$$\lim_{\xi \rightarrow \infty} \sigma_{\cos \theta}^2(\xi) = \frac{1}{3},$$

which is also a diffusion result. Thus, the asymptotic limits of the first two spatial and angular moments of the photon distribution are those of a diffusion process in an infinite medium. Furthermore, the diffusion limits are approximated after about $\xi = 15$, suggesting a diffusion (or thick cloud) regime for optical thicknesses greater than $\tau = 15$.

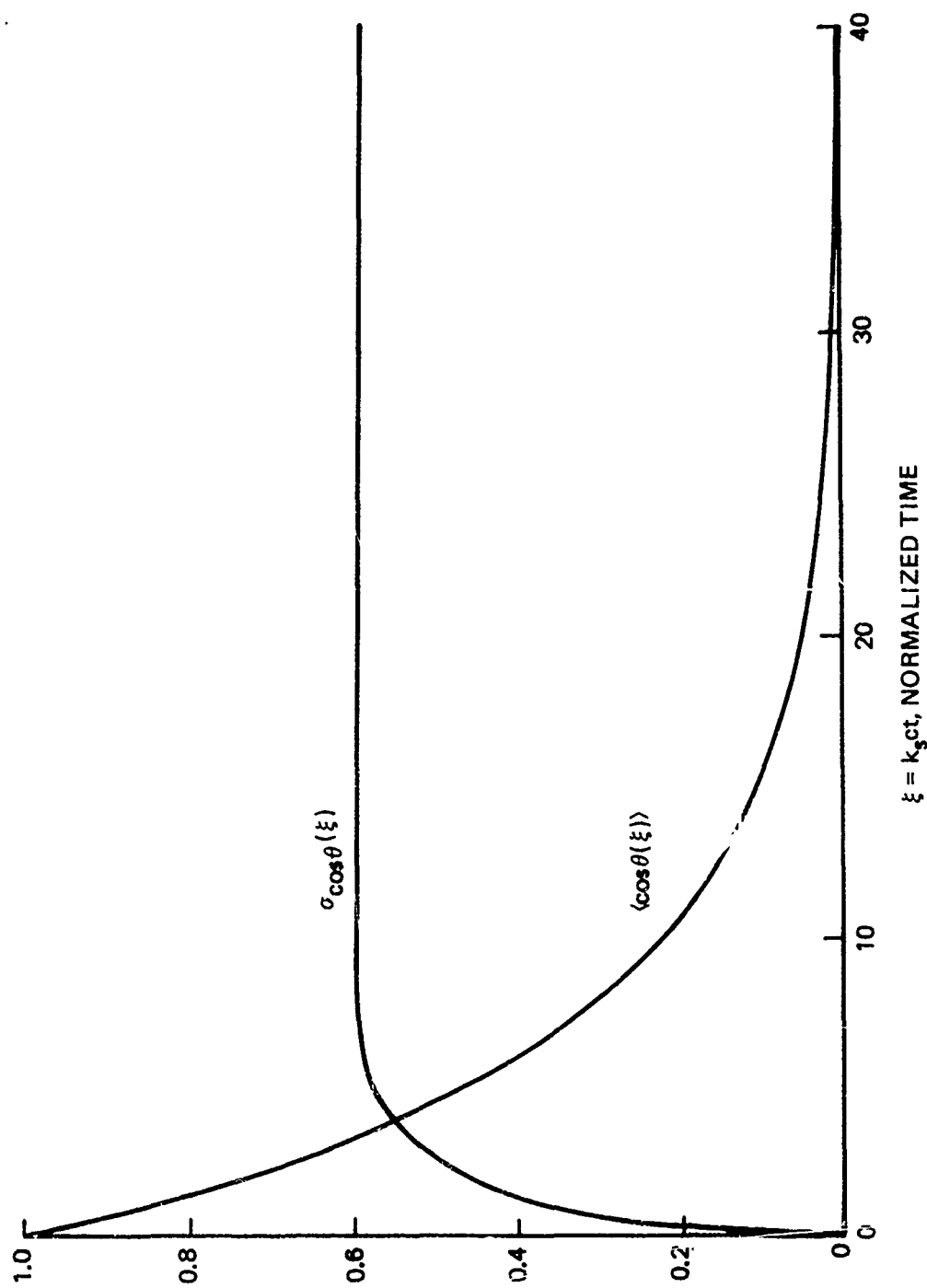


Fig. 5--First two angular moments for $\langle \cos \theta \rangle = \langle \cos^2 \theta \rangle = 0.850$

FORWARD SCATTER REGIME

Since photon scattering in clouds is highly peaked in the forward direction, photons deflected only a few times maintain their initial spatial, angular, and temporal cohesion. In our normalized units, the average number of scatterings at time ξ is ξ itself for randomly distributed aerosols. For small ξ , therefore, we would expect the moment formulae to evince the behavior attributed to the *multiple forward scatter* (or thin cloud) regime.

Expressing $\sigma_x^2(\xi)$ from Eq. (22) as a power series of ξ , we obtain

$$\sigma_x^2(\xi) = \frac{2w}{3(w-v)} \sum_{k=3}^{\infty} (-1)^k (v^{k-2} - w^{k-2}) \frac{\xi^k}{k!},$$

which provides the interesting small-time expression

$$\sigma_x^2(\xi) \cong \frac{w}{9} \xi^3. \quad (31)$$

The usual definition of mean square spread [3] results in

$$\begin{aligned} \langle r^2 \rangle &= \langle x^2 \rangle + \langle y^2 \rangle \\ &= 2\sigma_x^2(\xi) \\ &\cong \frac{2w}{9} \xi^3 \end{aligned} \quad (32)$$

for small times. When written in the dimensioned variables $R = k_s^{-1} r$ and $t = (k_s c)^{-1} \xi$, with the small-angle assumptions $\langle \cos^2 \theta \rangle \cong 1 - \langle \theta^2 \rangle$ and $ct \cong Z$, Eq. (32) becomes

$$\langle R^2 \rangle = \frac{1}{3} \lambda k_e Z^3 \langle \theta^2 \rangle,$$

which is identical to the small-angle scattering result (cf. [3] and [7]).

However, the dependence of $\langle r^2 \rangle$ on ξ^3 in the approximate equation (32) is valid for only about $\xi \leq 5$, as shown in Fig. 6, where the rms beam spread $\sqrt{\langle r^2 \rangle}$ is plotted using $\sigma_x^2(\xi)$ from both the exact equation (22) and the approximate (small time) equation (31). We thus conclude that, for calculating mean square spread, the small-angle assumption is questionable for optical thicknesses greater than $\tau = 5$.

The moment formulae also allow for a simplified calculation of the average multipath pulse delay for thin clouds. Let $\Delta\xi = \xi - \tau$ be the random delay between the time an unscattered photon passes through the plane $z = \tau$ (in normalized units, this time is τ itself since the normalized velocity is unity) and the random time ξ at which the possibly scattered photon passes through the plane $z = \tau$.

It is reasonable to estimate the average value of ξ as the time taken by the centroid of the photon density along the z -axis to pass through the $z = \tau$ plane. Thus, inverting Eq. (21) yields

$$\bar{\xi} \cong \frac{1}{v} \ln \left(\frac{1}{1 - v\tau} \right) ,$$

so

$$\overline{\Delta\xi} \cong \frac{1}{v} \ln \left(\frac{1}{1 - v\tau} \right) - \tau , \quad (33)$$

an expression that should be applicable for small τ .

Figure 7 plots Eq. (33) and the thick-cloud simulation curve fit [4] for $\overline{\Delta\xi}$ versus τ . The expression given by Eq. (33) appears to diverge from the simulation prediction (compared with a true cloud exit but for relatively large τ) at about $\tau = 5$, where backscatter starts to become important. The divergence arises because Eq. (33) for $\overline{\Delta\xi}$ is derived from an infinite cloud model, so photons that would have left a finite cloud tend to increase the time for the z -axis centroid to reach the plane $z = \tau$. For small τ , however, nearly all photons are heading in the forward (increasing z) direction, so the lack of a true cloud exit at τ is inconsequential.

An analysis based on a path-length integral along $r \sim z^{3/2}$ --the small-angle-derived, mean square, transverse spread--obtains the

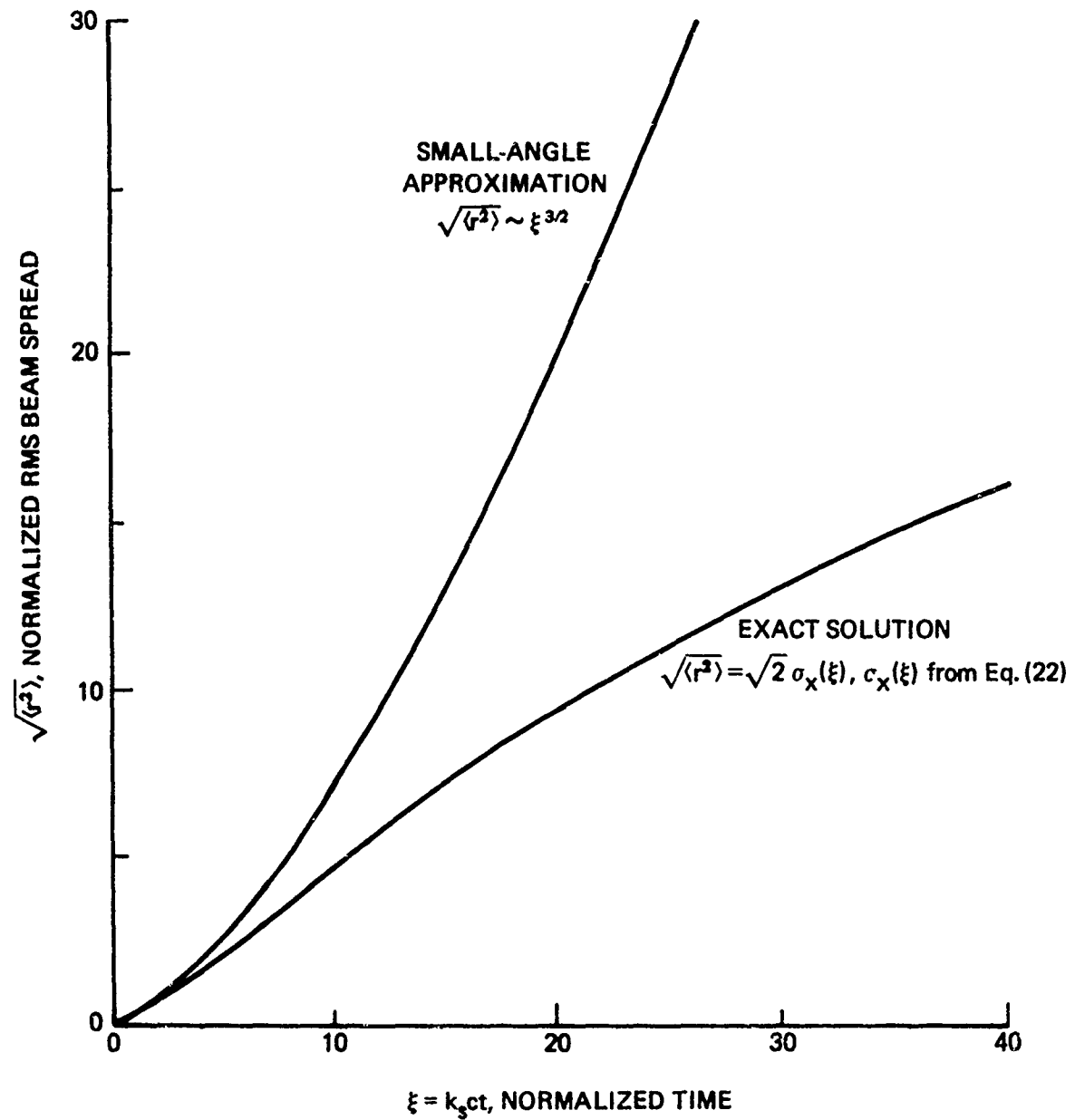


Fig. 6--Effects of small-angle assumption on rms beam spread

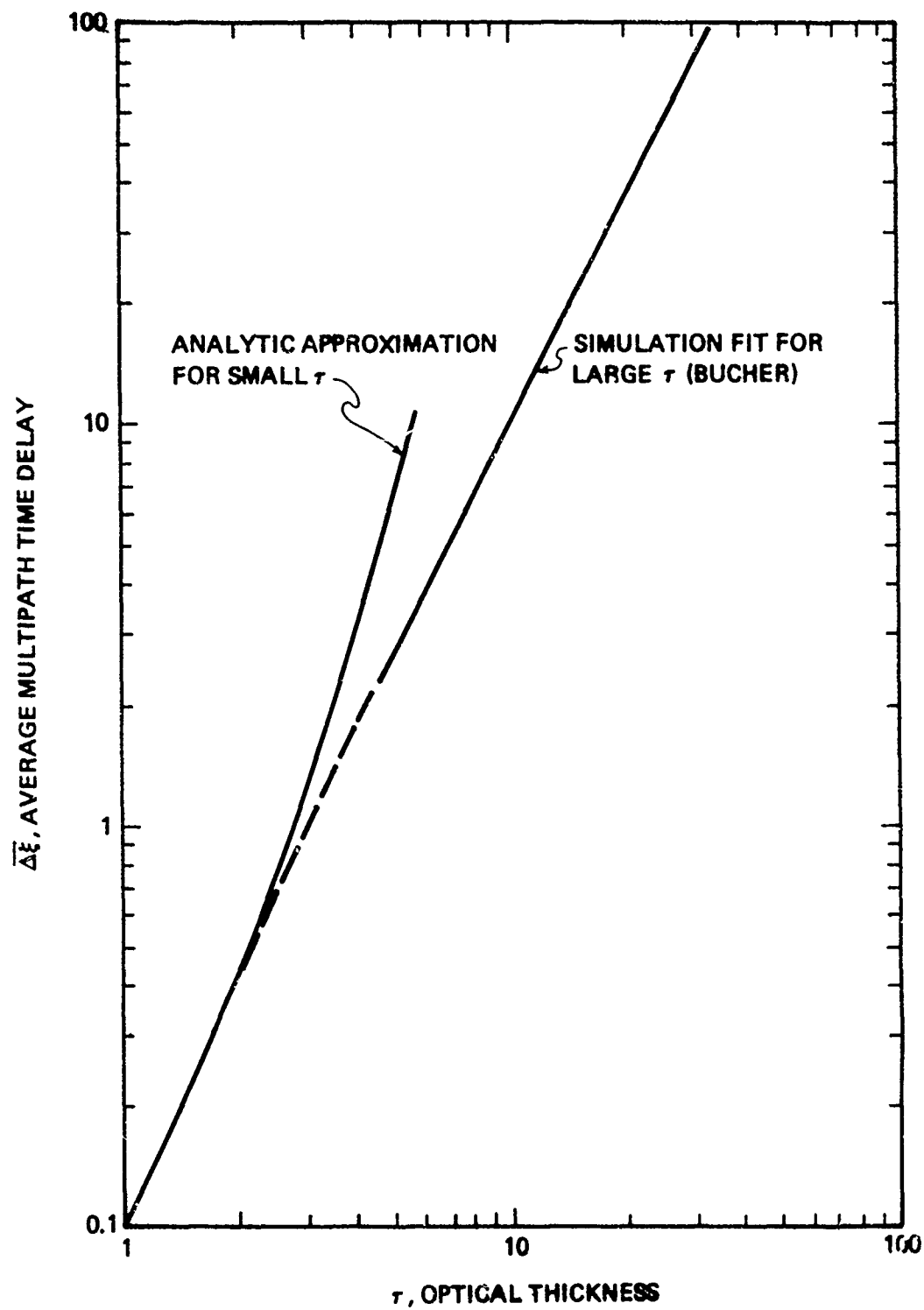


Fig. 7--Average multipath time delay for $\langle \cos \theta \rangle = 0.827$

expression [8] (in our notation with the single-scatter albedo set to unity)

$$\overline{\Delta\xi} = \tau\xi \frac{0.30}{\tau\langle\theta^2\rangle} \left[\left(1 + \frac{9}{4} \tau\langle\theta^2\rangle \right)^{3/2} - 1 \right] . \quad (34)$$

Expanding Eq. (34) in τ , and ignoring third and higher order terms, we obtain the small τ expression

$$\overline{\Delta\xi} = 0.57 \tau^2 \langle\theta^2\rangle . \quad (35)$$

Similarly expanding Eq. (33) and setting $v = 1 - \langle\cos\theta\rangle \cong \langle\theta^2/2\rangle$ yields

$$\overline{\Delta\xi} = \frac{1}{4} \tau^2 \langle\theta^2\rangle ,$$

about a factor of two less than Eq. (35). This discrepancy is apparently due to the path chosen to calculate $\overline{\Delta\xi}$ in Eq. (34) (i.e., $r \sim z^{3/2}$) being too long for photons that have suffered, on average, only τ scatterings. However, Eq. (34) eventually (for $\tau > 30$) yields an underestimate of $\overline{\Delta\xi}$ compared with simulation results (cf. [9]) because the smooth path is shorter than the jagged diffusion-like sample paths.

CONDITIONAL MOMENTS

Recall that intermediate results in the moment derivations of Sec. II are expressions for the moments conditioned on exactly n scatterings. The conditional moments provide physical insights into the scattering process that are not apparent from inspection of the unconditional moments. Hence, Fig. 8 plots $\bar{z}_n(\xi)$ from Eq. (8) and

$$\sigma_x(n, \xi) = [\langle x_n^2(\xi) \rangle]^{1/2} \quad \text{and} \quad \sigma_z(n, \xi) = [\langle z_n^2(\xi) \rangle - \bar{z}_n^2(\xi)]^{1/2}$$

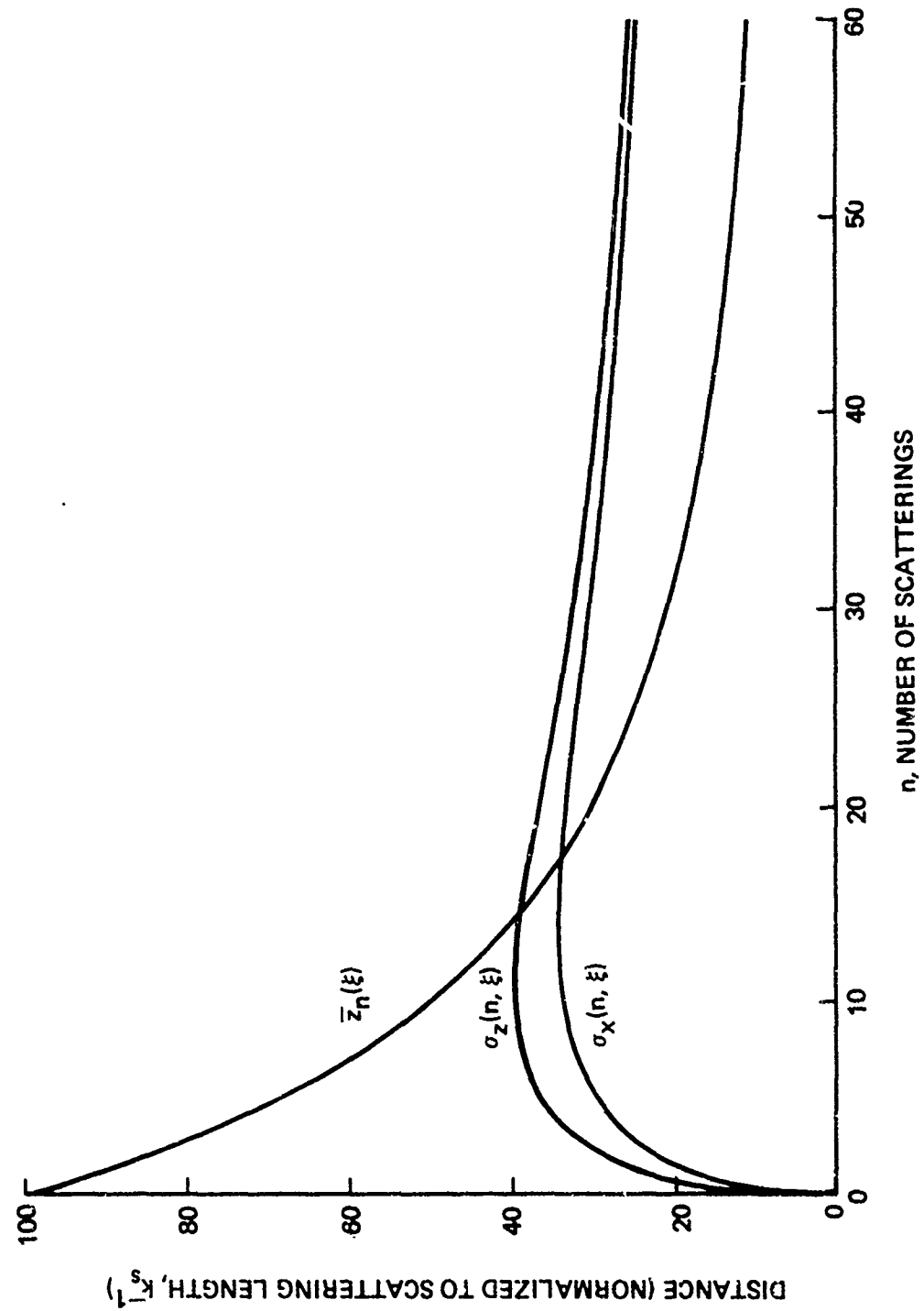


Fig. 8--Conditional spatial moments for $\langle \cos^2 \theta \rangle = 0.850$

from Eqs. (15) and (16), respectively. Although Fig. 8 is for $\xi = 100$, observe that $\bar{z}_n(\xi)$, $\sigma_x(n, \xi)$, and $\sigma_z(n, \xi)$ are all proportional to ξ --so, when considered as functions of n for fixed ξ , their form is invariant with ξ .

The behavior of $\bar{z}_n(\xi)$ in Fig. 8 is intuitive: the higher the scattering order n , the closer the centroid of the conditional distribution lies to the origin (indeed, $\lim_{n \rightarrow \infty} \bar{z}_n(\xi) = 0$). That is, on average, the more a photon is scattered, the farther it lags behind its unscattered brethren.

The plots of $\sigma_z(n, \xi)$ and $\sigma_x(n, \xi)$ display maxima at about $n = 10$ and $n = 15$, respectively. The values of n at which these maxima occur are sensitive to $\langle \cos \theta \rangle$ but invariant with ξ . Furthermore,

$\lim_{n \rightarrow \infty} \sigma_z(n, \xi) = \lim_{n \rightarrow \infty} \sigma_x(n, \xi) = 0$. Thus, at any time ξ , photons scattered many times tend to accumulate at the origin, their dispersion decreasing with order n . Such clustering occurs because, at a given time, all photons have the same path length but the relatively jagged (diffusion-like) paths of those that have been scattered many times will have, on average, kept them closer to the origin. That effect would be most pronounced for isotropic scattering (i.e., $\langle \cos \theta \rangle = 0$) since it is identical to diffusion in the limit of a decreasing mean free path between scatterings.

IV. DIFFUSION APPROXIMATION FOR MULTIPLE SCATTERING IN AN INFINITE CLOUD LAYER

The moments of the radiance distribution and the ultimately diffusive behavior of scattered photons are now used to develop an expression for the irradiance at the exit of an infinite plane-parallel cloud. The irradiance allows us to calculate the power collected over an infinite plane receiver at the cloud exit, then compare our results with Monte Carlo simulations of the identical problem. The calculated and simulated power pulses strongly agree for $\tau = 30$ and are virtually indistinguishable for $\tau = 80$.

DIFFUSION EQUATION

The three-dimensional diffusion equation for a particle with homogeneous diffusion coefficient $\underline{D}(\xi) = (D_x(\xi), D_y(\xi), D_z(\xi))^T$, drift coefficient $\underline{a}(\xi) = (a_x(\xi), a_y(\xi), a_z(\xi))^T$, and absorption coefficient κ is [10]*

$$\frac{\partial \rho(\underline{x}, \xi)}{\partial \xi} = \left[\frac{\underline{D}(\xi)}{2} \cdot \left(\frac{\partial^2}{\partial \underline{x}^2} \right) - \underline{a}(\xi) \cdot \left(\frac{\partial}{\partial \underline{x}} \right) - \kappa \right] \rho(\underline{x}, \xi), \quad (36)$$

where $\rho(\underline{x}, \xi)$ is the probability volume density for the particle at time ξ . The solution of Eq. (36) for a particle initially at the origin ($\rho(\underline{x}, 0) = \delta(\underline{x})$) in an infinite homogeneous medium is given by [10]

$$\rho(\underline{x}, \xi) = (2\pi)^{-3/2} \Lambda^{-1} \exp \left\{ -[\kappa \xi + (2\Lambda)^{-1} (\underline{x} - \mu)^T (\underline{x} - \mu)] \right\}, \quad (37)$$

*

For simplicity, we define $\frac{\partial}{\partial \underline{x}} = \left(\frac{\partial}{\partial x}, \frac{\partial}{\partial y}, \frac{\partial}{\partial z} \right)^T$ and

$$\frac{\partial^2}{\partial \underline{x}^2} = \left(\frac{\partial^2}{\partial x^2}, \frac{\partial^2}{\partial y^2}, \frac{\partial^2}{\partial z^2} \right)^T.$$

where

$$\underline{u} = \int_0^{\xi} \underline{a}(\xi') d\xi'$$

and

$$\Lambda = \int_0^{\xi} D_x(\xi') d\xi' \int_0^{\xi} D_y(\xi') d\xi' \int_0^{\xi} D_z(\xi') d\xi' .$$

Equation (37) is simply the product of three independent Gaussian densities and an absorption term $e^{-\kappa\xi}$. Hence we may write

$$\rho(x, \xi) = e^{-\kappa\xi} \rho_x(x, \xi) \rho_y(y, \xi) \rho_z(z, \xi) ,$$

where ρ_x , ρ_y , and ρ_z are one-dimensional Gaussian densities. Since a Gaussian density is determined by its first two moments and the moments of the transport process in an infinite medium were derived in Sec. II, we conclude that

$$\underline{a}(\xi) \simeq \frac{\partial \underline{x}(\xi)}{\partial \xi} = \left(0, 0, \frac{\partial \bar{z}(\xi)}{\partial \xi} \right)^T \quad (38)$$

and

$$\underline{D}(\xi) \simeq \left(\frac{\partial \sigma_x^2(\xi)}{\partial \xi}, \frac{\partial \sigma_y^2(\xi)}{\partial \xi}, \frac{\partial \sigma_z^2(\xi)}{\partial \xi} \right)^T , \quad (39)$$

where $\bar{z}(\xi)$, $\sigma_x^2(\xi) = \sigma_y^2(\xi)$, and $\sigma_z^2(\xi)$ are given by Eqs. (21), (22), and (24), respectively.

Recall that Sec. III shows that $\bar{z}(\xi)$, $\sigma_x^2(\xi)$, and $\sigma_z^2(\xi)$ asymptotically approach classical diffusion limits. Although the nonstationary transport equation (1) has been approximated by the diffusion equation (36) in prior treatments (cf. [11] and [12]), the drift and diffusion coefficients have been time-invariant--generally set equal to their

asymptotic values or otherwise approximated. Armed with the exact closed-form expressions derived in Sec. II, we will strive to extend the region of validity for the diffusion approximation by employing the "correct" time-varying coefficients. In the simplest sense, Eqs. (37) through (39) together constitute the correct Green's function for the photon density of the infinite-medium transport problem because they provide the correct spatial moments for all $\xi > 0$. However, the diffusion approximation used to obtain that solution forces the density $\rho(\underline{x}, \xi)$ into a Gaussian form that is valid only after the onset of the diffusion regime ($\xi \geq 15$).

BOUNDARY CONDITIONS

Consider a photon that traverses the boundary between a scattering and a nonscattering medium. Since it can never return to the scattering medium, its behavior inside the cloud may be likened to that of a diffusing particle attaining an absorbing wall. Diffusion theory provides the absorbing-wall boundary condition $\rho(\underline{x}, \xi) = 0$ for all \underline{x} along the wall [10]. However, close to boundaries, the diffusion approximation to the transport process is known to be questionable.

By direct solution of Milne's equation for a simpler, related problem, Morse and Feshbach [11] have shown that the appropriate condition for a diffusing particle used to approximate photon transport across an exit boundary is given by

$$\rho_z(z) \approx 0.71 \left. \frac{\partial \rho}{\partial z} \right|_{z=0 \text{ or } z=\tau}, \quad (40)$$

where, as shown in Fig. 1, we have modeled our cloud as a slab of infinite horizontal extent and (optical) thickness $\tau = k_s Z_0 - Z_0$ being the physical thickness of the cloud. Since Milne's problem considers a stationary plane wave incident on the scattering medium, Eq. (40) is the steady-state boundary condition for a three-dimensional problem that reduces to one dimension by symmetry. Furthermore, Eq. (40) holds for only *isotropic* scattering, suggesting that the usual $v = 1 - \langle \cos \theta \rangle$

scaling for anisotropic scattering [11-13] should be applied to obtain the boundary condition

$$\rho_z(z) = \frac{0.71}{v} \frac{\partial \rho_z}{\partial z} \bigg|_{z=0 \text{ or } z=\tau}, \quad (41)$$

which we use below.

The difficulty in applying Eq. (41) lies in specification of both the density and its gradient at the boundary. Adopting the technique of Morse and Feshbach [11,12], we extend the scattering medium a distance $0.71/v$ beyond each boundary and set $\rho_z(z, \xi) \equiv 0$ at the boundary of the extended medium, as represented in Fig. 9. Using the extended medium with the diffusion approximation for Milne's steady-state problem results in an error of no more than a 0.3 percent for ρ_z in the scattering medium, compared with the exact solution [11].

We now solve Eq. (36) with the coefficients from Eqs. (38) and (39), initial condition

$$\rho(\underline{x}, \xi) = \delta(x) \delta(y) \delta(z), \quad \xi = 0 \quad (42)$$

and boundary conditions

$$\rho(\underline{x}, \xi) \equiv 0, \quad z = -\frac{0.71}{v} \text{ and } z = \tau + \frac{0.71}{v} \quad (43)$$

and

$$\rho(\underline{x}, \xi) \equiv 0, \quad x = y = \pm \infty. \quad (44)$$

The separability of the initial and boundary conditions for Eq. (36) implies that the solution is of the form

$$\rho(\underline{x}, \xi) = e^{-K\xi} \rho_x(x, \xi) \rho_y(y, \xi) \rho_z(z, \xi), \quad (45)$$

where ρ_x , ρ_y , and ρ_z are the solutions to three one-dimensional diffusion equations with the corresponding one-dimensional boundary

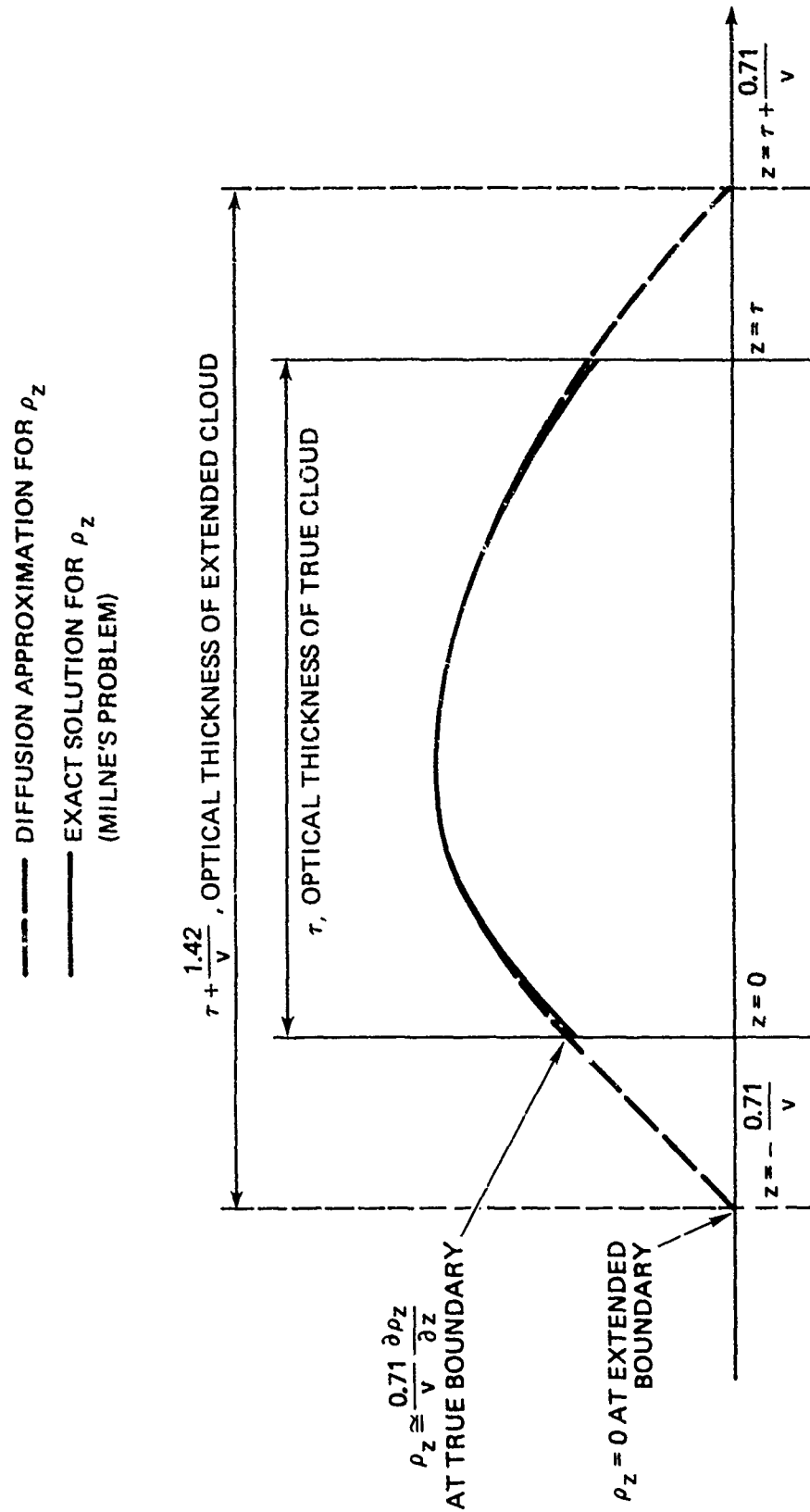


Fig. 9--Representation of photon density $\rho_z(z, \xi)$, ξ fixed, using diffusion theory approximation with extended cloud boundary condition

conditions and without an absorption term [14]. Thus, ρ_x and ρ_y remain Gaussian with mean zero and variance $\sigma_x^2(\xi) = \sigma_y^2(\xi)$ given by Eq. (22), since our finite-thickness cloud is still of infinite horizontal extent. Hence

$$\rho_x(x, \xi) = \frac{1}{\sigma_x \sqrt{2\pi}} \exp \left[-\frac{x^2}{2\sigma_x^2(\xi)} \right] \quad (46)$$

and

$$\rho_y(y, \xi) = \frac{1}{\sigma_y \sqrt{2\pi}} \exp \left[-\frac{y^2}{2\sigma_y^2(\xi)} \right] . \quad (47)$$

For $\rho_z(z, \xi)$, we seek the solution of

$$\frac{\partial \rho_z}{\partial \xi} = \frac{D_z(\xi)}{2} \frac{\partial^2 \rho_z}{\partial z^2} - a_z(\xi) \frac{\partial \rho_z}{\partial z} \quad (48)$$

subject to

$$\rho_z(z, \xi) = \delta(z) , \quad \xi = 0$$

and

$$\rho_z(z, \xi) \equiv 0 , \quad z = -\frac{0.71}{v} \text{ and } z = \tau + \frac{0.71}{v} .$$

The method of images obtains the solution [14]

$$\begin{aligned} \rho_z(z, \xi) = & \frac{1}{\sigma_z(\xi) \sqrt{2\pi}} \sum_{k=-\infty}^{\infty} \left[\exp \left\{ -\left[z - \bar{z}(\xi) + 2k \left(\tau + \frac{1.42}{v} \right) \right]^2 \right\} \right. \\ & \left. - \exp \left\{ -\left[z + \bar{z}(\xi) + 2k \left(\tau + \frac{1.42}{v} \right) + \frac{1.42}{v} \right]^2 \right\} \right] , \quad (49) \end{aligned}$$

which is a rapidly converging series for all z and ξ of interest. Thus, the solution of Eq. (36) with coefficients given by Eqs. (38) and (39), initial condition by Eq. (42), and boundary conditions by Eqs. (43) and (44) is

$$\rho(\underline{x}, \xi) = e^{-\kappa \xi} \rho_x(x, \xi) \rho_y(y, \xi) \rho_z(z, \xi) ,$$

where ρ_x , ρ_y , and ρ_z are given by Eqs. (46), (47), and (49), respectively. The absorption coefficient κ , normalized to the mean free scattering length k_s^{-1} , is

$$\kappa = \frac{k_a}{k_s} = \frac{1 - \lambda}{\lambda} , \quad (50)$$

where k_a is the unnormalized absorption coefficient and λ is the single-scatter albedo.

IRRADIANCE AT CLOUD EXIT

Consider the probability that an unabsorbed photon initially at $\underline{x} = 0$ has left the scattering medium by time ξ . This probability is given in the diffusion approximation by the cumulative probability that a diffusing particle remains unabsorbed in the medium until time ξ :

$$\begin{aligned} \mathcal{P}\{z(\xi) \in [0, \tau]\} &= 1 - \int_{x=-\infty}^{\infty} \int_{y=-\infty}^{\infty} \int_{z=0}^{\tau} e^{\kappa \xi} \rho(\underline{x}, \xi) dV_{\underline{x}} \\ &= 1 - \int_{x=-\infty}^{\infty} \int_{y=-\infty}^{\infty} \int_{z=0}^{\tau} \rho_x(x, \xi) \rho_y(y, \xi) \rho_z(z, \xi) dx dy dz \\ &= 1 - \int_0^{\tau} \rho_z(z, \xi) dz . \end{aligned}$$

We can thus use Eq. (48) to obtain the exit time (or "first passage") density

$$\begin{aligned} \frac{\partial}{\partial \xi} \mathcal{P}\{z(\xi) \in [0, \tau]\} &= 1 - \int_0^\tau \frac{\partial \rho_z}{\partial \xi} dz \\ &= - \int_0^\tau \left[\frac{D_z(\xi)}{z} \frac{\partial^2 \rho_z}{\partial z^2} - a_z(\xi) \frac{\partial \rho_z}{\partial z} \right] dz \\ &= \left[a_z(\xi) \rho_z - \frac{D_z(\xi)}{2} \frac{\partial \rho_z}{\partial z} \right]_{z=\tau} - \left[a_z(\xi) \rho_z - \frac{D_z(\xi)}{2} \frac{\partial \rho_z}{\partial z} \right]_{z=0}. \end{aligned}$$

The first term in the last expression is the first-passage probability density for photons leaving the cloud (bottom) at $z = \tau$. That density is recognizable as the usual diffusion flux

$$\frac{D_z}{2} \nabla_z \rho_z$$

augmented by a drift term $a_z \rho_z = e^{-v\xi} \rho_z$ [from Eqs. (21) and (38)], which quickly expires for optically thick clouds. Denoting the first-passage density at the cloud bottom by $A(\tau, \xi)$, we have

$$\begin{aligned} A(\tau, \xi) &= \left[e^{-v\xi} \rho_z - \frac{D_z(\xi)}{2} \frac{\partial \rho_z}{\partial z} \right]_{z=\tau} \\ &= \frac{1}{\sigma_z(\xi) \sqrt{2\pi}} \sum_{k=-\infty}^{\infty} \left\{ \exp \left[-\frac{\beta_1^2}{2\sigma_z^2(\xi)} \right] \left[e^{-v\xi} + \frac{D_z(\xi)}{2\sigma_z^2(\xi)} \beta_1 \right] \right. \\ &\quad \left. - \exp \left[-\frac{\beta_2^2}{2\sigma_z^2(\xi)} \right] \left[e^{-v\xi} + \frac{D_z(\xi)}{2\sigma_z^2(\xi)} \beta_2 \right] \right\}, \end{aligned} \quad (51)$$

where

$$\beta_1 = -\bar{z}(\xi) + \tau(1 + 2k) + 4k \left(\frac{0.71}{v} \right),$$

$$\beta_2 = \bar{z}(\xi) + (1 + 2k) \left(\tau + \frac{1.42}{v} \right),$$

and, from Eq. (24),

$$D_z(\xi) = \frac{2\sigma_z^2(\xi)}{\partial \xi} = \frac{2}{v} \left[\frac{(w - 3v)(1 - e^{-v\xi}) + 2v(1 - e^{-w\xi})}{3(w - v)} - e^{-v\xi}(1 - e^{-v\xi}) \right].$$

Thus, for a narrow, collimated, delta-pulse source with energy E_0 , we obtain from Eq. (51) the irradiance on the exit plane $z = \tau$ as

$$J(r, \tau; \xi) = E_0 e^{-\kappa\xi} \rho_r(r, \xi) A(\tau, \xi), \quad (52)$$

where the radial distance $r = (x^2 + y^2)^{1/2}$. Since x and y are Gaussian random variables, r is Rayleigh-distributed, so

$$\rho_r(r, \xi) = \frac{r}{\sigma_x^2(\xi)} \exp \left[-\frac{r^2}{2\sigma_x^2(\xi)} \right]. \quad (53)$$

COMPARISON WITH MONTE CARLO SIMULATIONS

Now we digress to test the validity of Eq. (52). Consider the power into an infinite-plane, $\pi/2$ -field-of-view receiver. For $E_0 = 1$ and $\kappa = 0$, the received power pulse is simply $A(\tau, \xi)$ since, from Eq. (52),

$$\int_{r=0}^{\infty} J(r, \tau; \xi) dr = A(\tau, \xi) \int_0^{\infty} \rho_r(r, \xi) dr \equiv A(\tau, \xi).$$

Bucher [4] considers this problem in his Monte Carlo simulations. Figures 10 and 11 plot the simulated and calculated pulses for $\tau = 30$ and 80, respectively. Although the pulse amplitudes have been normalized to unity in these figures, the integral of the pulses, or received energy,

$$E_{\tau} = \int_0^{\infty} A(\tau, \xi) d\xi ,$$

also agrees well with Bucher's Monte Carlo curve fit, as shown in Fig. 12.

Bucher also plots $\langle r \rangle_{\tau}$, the mean radial distance of exiting photons for a cloud of optical thickness τ . We calculate

$$\langle r \rangle_{\tau} = \int_0^{\infty} r h_{\tau}(r) dr , \quad (54)$$

where $h_{\tau}(r) dr$ is the conditional probability of a photon exiting through an annulus dr at r given that it attains $z = \tau$. Defining B as the event corresponding to the photon leaving at all, and using conditional probabilities, we have

$$\begin{aligned} h_{\tau}(r) dr &= \mathcal{P}\{r \in dr/B\} = \mathcal{P}\{r \in dr, B\}/\mathcal{P}\{B\} \\ &= \int_{\xi=0}^{\infty} \mathcal{P}\{r \in dr, \xi \in d\xi, B\}/\mathcal{P}\{B\} \\ &= \int_{\xi=0}^{\infty} \mathcal{P}\{r \in dr, B/\xi\} \mathcal{P}\{\xi \in d\xi, B\}/\mathcal{P}\{B\} . \end{aligned} \quad (55)$$

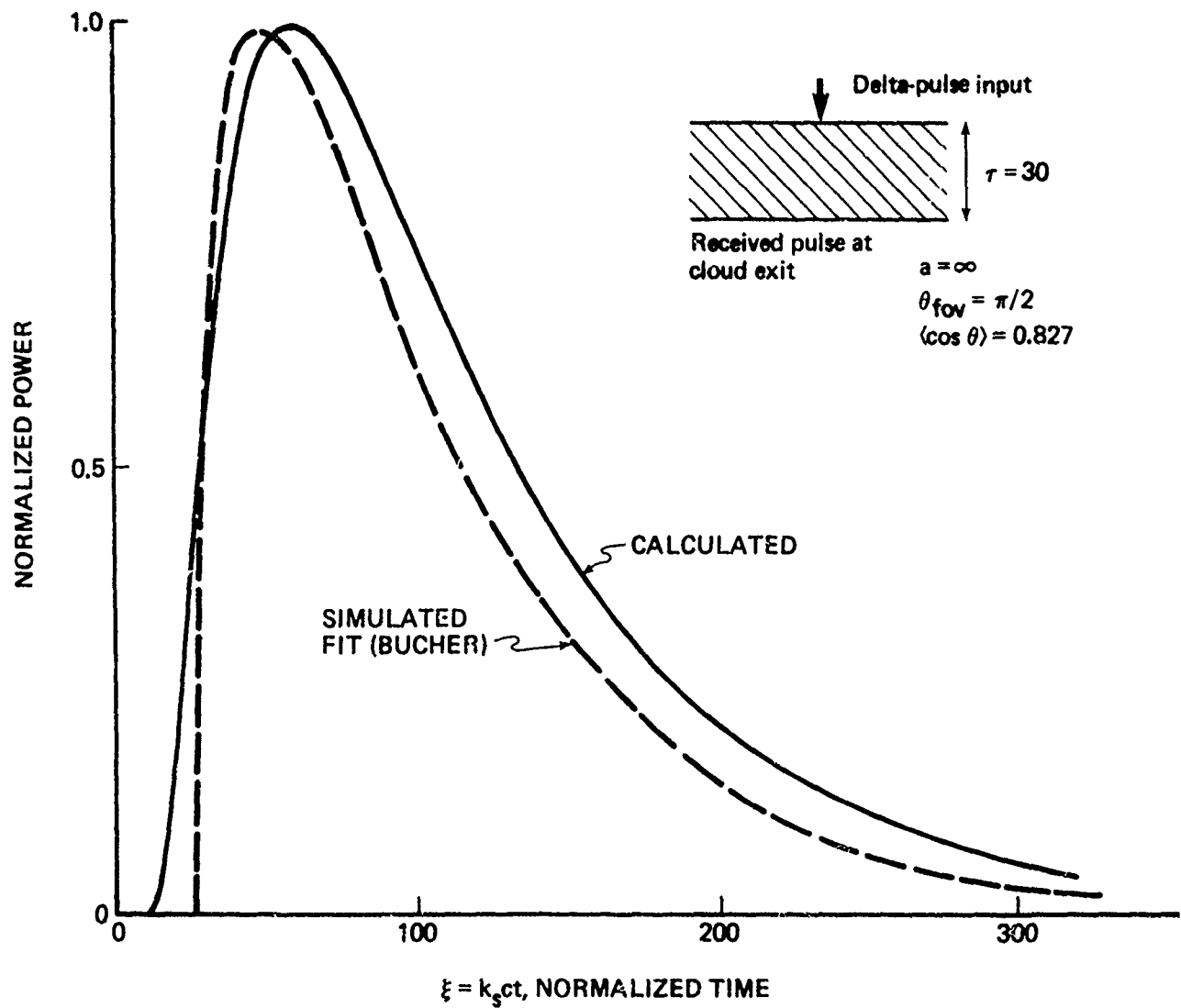


Fig. 10--Comparison of simulated and calculated power pulses for $\tau = 30$

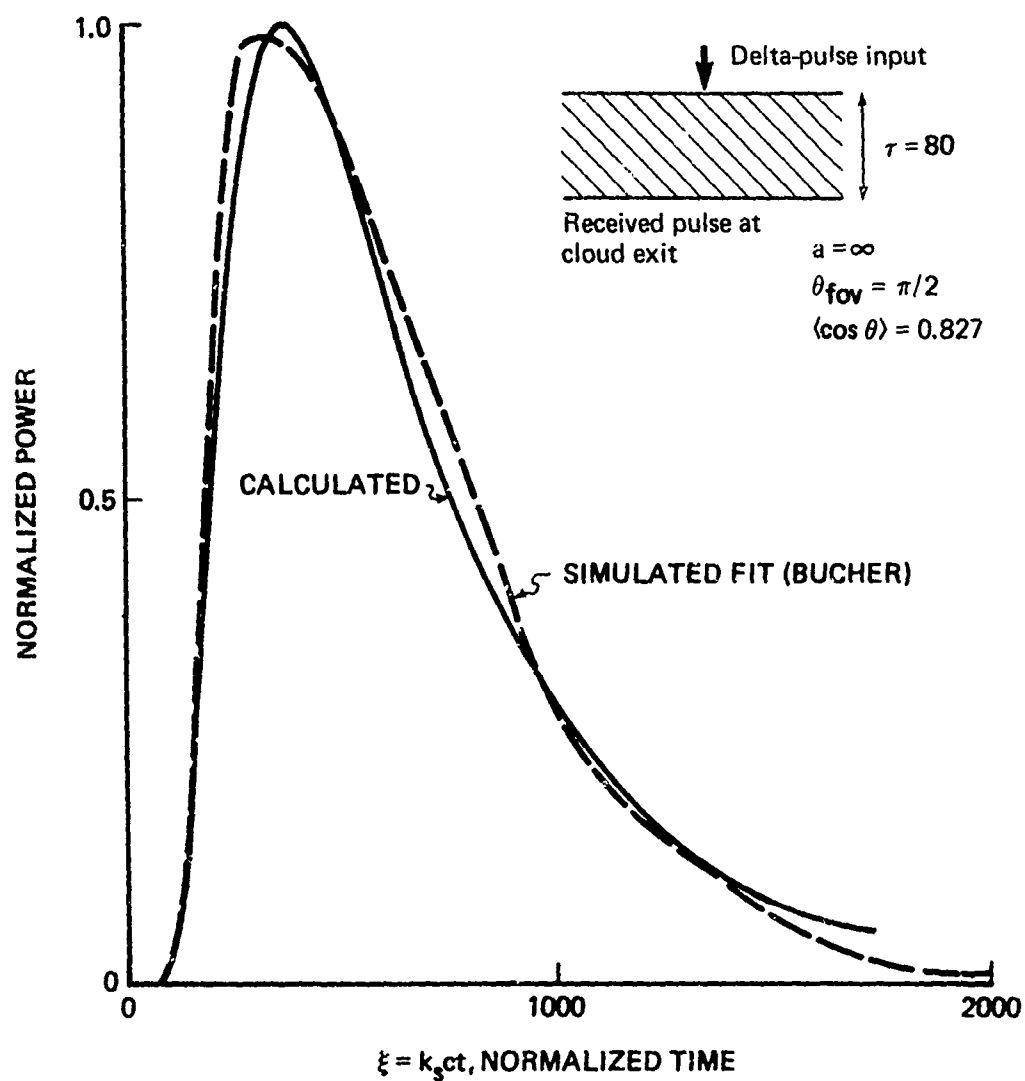


Fig. 11--Comparison of simulated and calculated power pulses for $\tau = 80$

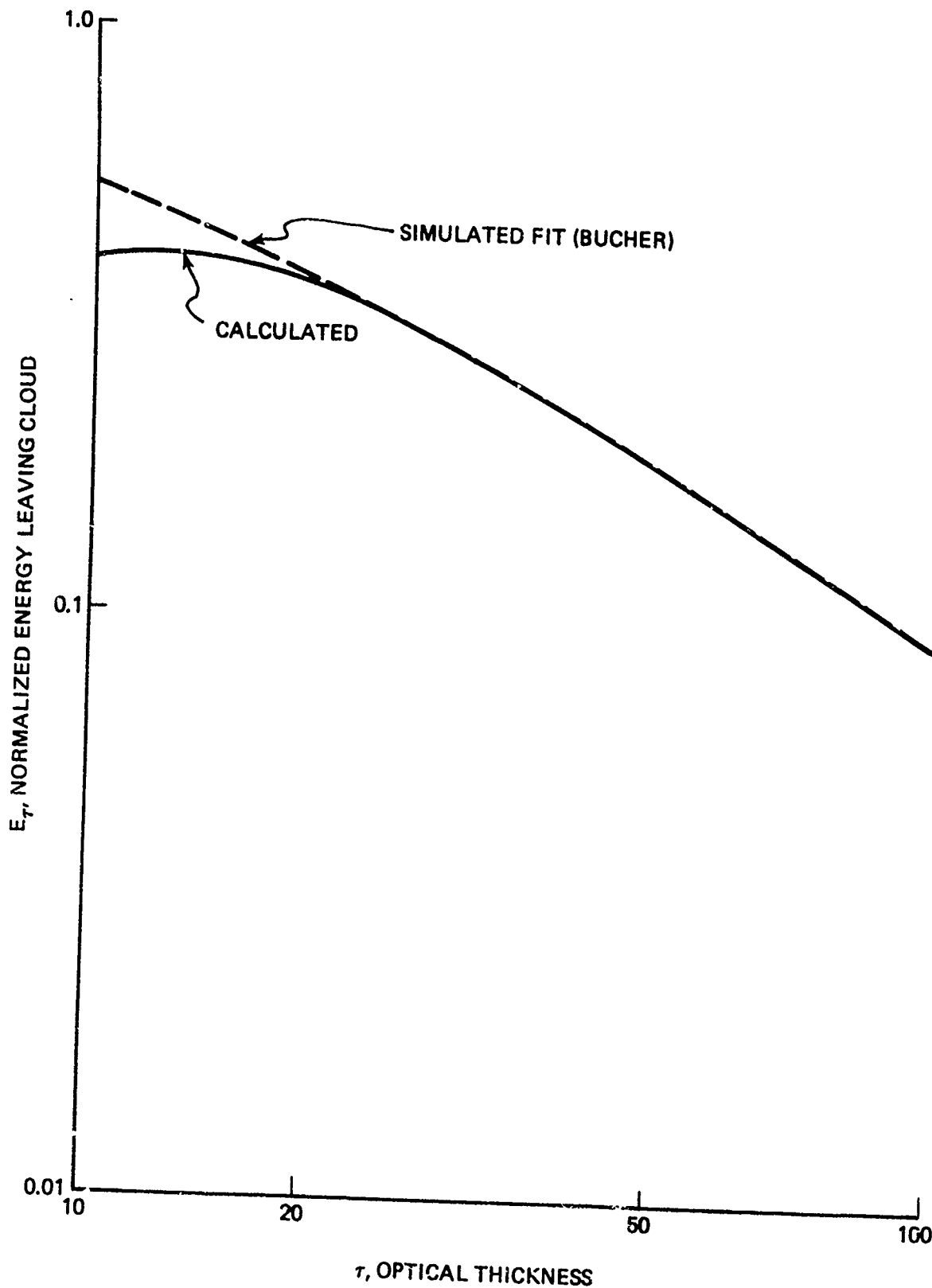


Fig. 12--Comparison of simulated and calculated energy transmission versus optical thickness for $\langle \cos \theta \rangle = 0.827$

But, from Eq. (53), the radial density of photons at time ξ is

$$\mathcal{P}\{r \in dr, B/\xi\} = \frac{r}{\sigma_x^2(\xi)} \exp \left[-\frac{r^2}{2\sigma_x^2(\xi)} \right]$$

and

$$\mathcal{P}\{B\} = \int_0^\infty A(\tau, \xi) d\xi = E_\tau .$$

After substitution, Eq. (55) becomes

$$h_\tau(r) dr = E_\tau^{-1} \int_0^\infty \frac{r}{\sigma_x^2(\xi)} \exp \left[-\frac{r^2}{2\sigma_x^2(\xi)} \right] A(\tau, \xi) d\xi$$

and Eq. (54) is then

$$\langle r \rangle_\tau = E_\tau^{-1} \int_{r=0}^\infty \int_{\xi=0}^\infty \frac{r^2}{\sigma_x^2(\xi)} \exp \left[-\frac{r^2}{2\sigma_x^2(\xi)} \right] A(\tau, \xi) d\xi .$$

Reversing the order of integration and recognizing the Maxwellian density results in

$$\begin{aligned} \langle r \rangle_\tau &= E_\tau^{-1} \sqrt{\pi/2} \int_{\xi=0}^\infty \left\{ \int_{r=0}^\infty \frac{r^2}{\sigma_x^2(\xi)} \exp \left[-\frac{r^2}{2\sigma_x^2(\xi)} \right] dr \right\} \sigma_x(\xi) A(\tau, \xi) d\xi \\ &= E_\tau^{-1} \sqrt{\pi/2} \int_{\xi=0}^\infty \sigma_x(\xi) A(\tau, \xi) d\xi , \end{aligned} \quad (56)$$

which is numerically integrated and plotted with the Bucher curve fit in Fig. 13.

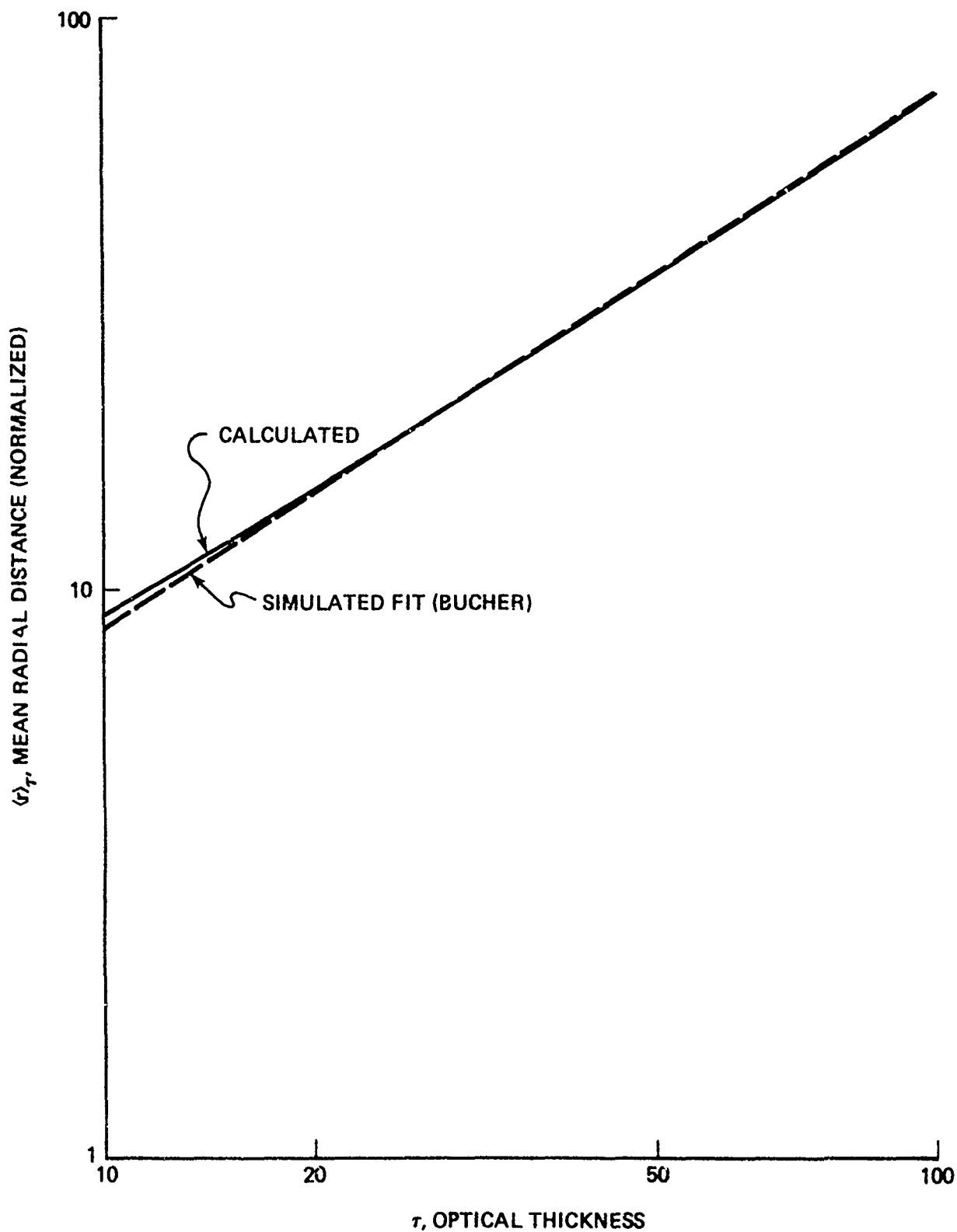


Fig. 13--Comparison of simulated and calculated mean radial distance of emerging photons versus optical thickness for $\langle \cos \theta \rangle = 0.827$

A key factor in optical communications, pulse stretching is dramatically affected by multipath delays due to multiple scattering in clouds, as shown in Figs. 10 and 11. To characterize multipath delay we again adopt the mean delay $\overline{\Delta\xi} = \overline{\xi} - \tau$ (discussed in Sec. III, p. 29). In the diffusion approximation for an infinite plane receiver at $z = \tau$,

$$\overline{\Delta\xi} = \frac{\int_{\xi=0}^{\infty} \xi A(\tau, \xi) d\xi}{\int_{\xi=0}^{\infty} A(\tau, \xi) d\xi} - \tau. \quad (57)$$

Figure 14 plots $\overline{\Delta\xi}$ against τ using Eq. (57) and the Bucher simulation curve. The calculated pulse broadens as the diffusion approximation breaks down below $\tau \approx 15$.

Together, Figs. 10 through 14 illustrate the remarkable correspondence between the calculated and the simulated results. The power of an analytic solution of the nonstationary transport problem does not, however, lie in duplicating highly aggregated simulation results. Rather, once validated, the analytic model provides solutions to problems that would require excessive computer time to simulate because of sparse histogram data. For example, if the infinite-plane, $\pi/2$ -field-of-view receiver is replaced by a finite receiver to study field-of-view effects, then an analytic treatment may provide the only practical way to obtain results. We consider the problem of finite receivers below.

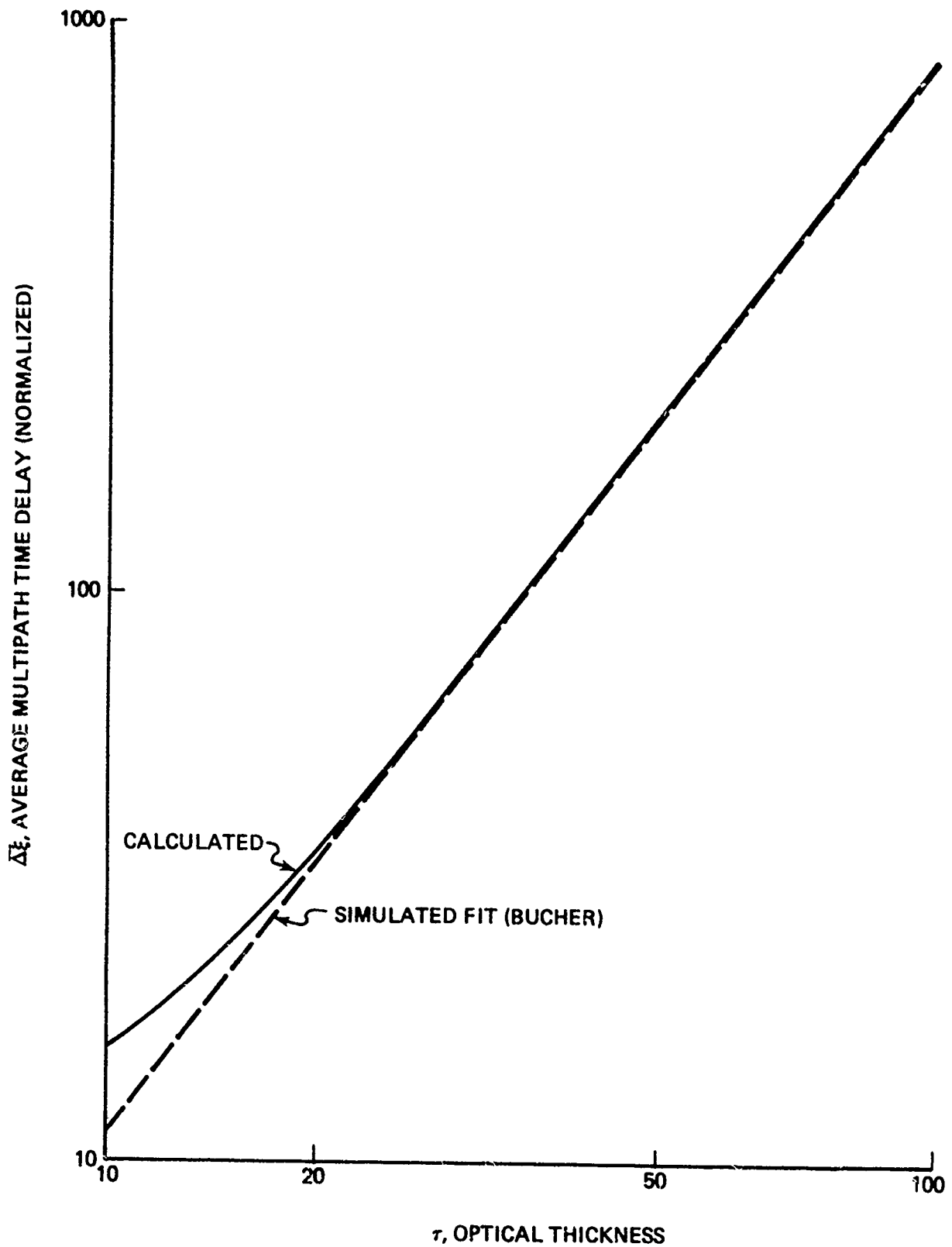


Fig. 14--Comparison of simulated and calculated average multipath time delay versus optical thickness for $\langle \cos \theta \rangle = 0.827$

V. PROPAGATION BELOW CLOUD AND FINITE RECEIVER CALCULATIONS

Recall that $J_\delta(r, \tau; \xi)$ in Eq. (52) is the diffusion-derived irradiance on the cloud exit plane ($z = \tau$) for an initial, narrow, collimated delta pulse at $\underline{x} = 0$ on the cloud entrance plane. The radiant source for the transport equation (1) in that case is

$$S_0(\underline{x}, \alpha; \xi) = \frac{E_0 \delta(\underline{x}) \delta(\alpha) \delta(\xi)}{\sin \theta},$$

where $\alpha = (\theta, \phi)$ denotes the ordered pair of polar and rotation angles, respectively. The generalization to a broad Gaussian beam at the cloud entrance with spatial variance σ_B^2 is straightforward. Hence, for the transport source

$$S_0(\underline{x}, \alpha; \xi) = \frac{E_0 \delta(z) \delta(\alpha) \delta(\xi)}{2\pi\sigma_B^2 \sin \theta} \exp \left[-\frac{(x^2 + y^2)}{2\sigma_B^2} \right], \quad (58)$$

or for the corresponding initial energy density in $r = (x^2 + y^2)^{1/2}$ and z

$$\rho(r, z, \xi) = E_0 r \sigma_B^{-2} \delta(z) \delta(\xi) \exp \left[-\frac{r^2}{2\sigma_B^2} \right], \quad (59)$$

the exit plane irradiance becomes

$$\begin{aligned} J(r, \tau; \xi) &= E_0 \int_0^\infty J_\delta(r - \mu, \tau; \xi) \frac{\mu}{\sigma_B^2} \exp \left[-\frac{\mu^2}{2\sigma_B^2} \right] d\mu \\ &= E_0 e^{-\kappa\xi} \rho_r(r, \xi) A(\tau, \xi), \end{aligned} \quad (60)$$

where

$$\rho_r(r, \xi) = \frac{r}{\sigma_x^2(\xi) + \sigma_B^2} \exp \left\{ -\frac{r^2}{2[\sigma_x^2(\xi) + \sigma_B^2]} \right\} \quad (61)$$

and $A(\tau, \xi)$ is given by Eq. (51). The broad-beam irradiance equation (60) is used below to develop an expression for the full radiance distribution at the cloud exit.

RADIANCE AND RECEIVED POWER AT CLOUD EXIT

The angular distribution of particles emitted from the exit surface of a plane-parallel scattering medium with a stationary plane-wave input (Milne's problem) is closely approximated by the normalized expression

$$g(\alpha) = \frac{2 + 3 \cos \theta}{7\pi}, \quad 0 \leq \theta \leq \pi/2, \quad 0 \leq \phi \leq 2\pi, \quad (62)$$

which is derived by Morse and Feshbach [11] using a steady-state diffusion approximation. Simulations for delta-pulse inputs have shown that the light emerging from an optically thick medium is consistent with Eq. (62) and nearly independent of r , τ , and ξ [4,15]. Thus, we adopt Eq. (62) for the angular distribution of photons leaving the bottom of the cloud, with the source function given by Eq. (58).

The separability of the spatial and angular dependence for light emerging from the cloud bottom implies a radiance of the form $I(r, \tau, \alpha; \xi) \sim J(r, \tau; \xi) g(\alpha)$. But, by definition,

$$J(r, \tau; \xi) = \int_{\Omega} I(r, \tau, \alpha; \xi) \cos \theta \, d\omega_{\alpha}, \quad (63)$$

where $d\omega_{\alpha} = \sin \theta \, d\theta \, d\phi$ is the solid-angle element in the direction $\alpha = (\theta, \phi)$, and the integral is over $\Omega = 4\pi$ steradians. With the initial condition given by Eq. (58), therefore, the radiance at the cloud exit from Eqs. (60), (62), and (63) is

$$\begin{aligned}
 I(r, \tau, \alpha; \xi) &= \frac{J(r, \tau; \xi) g(\alpha)}{\int_{\Omega} g(\alpha) \cos \theta d\omega_{\alpha}} \\
 &= \frac{E_0}{4\pi} e^{-\kappa \xi} (2 + 3 \cos \theta) \rho_r(r, \xi) \\
 &\quad \times A(\tau, \xi), \quad 0 \leq \theta \leq \pi/2, \quad (64)
 \end{aligned}$$

where $\rho_r(r, \xi)$ and $A(\tau, \xi)$ are given by Eqs. (61) and (51), respectively.

The power into an on-axis receiver at the cloud exit, with normalized aperture radius a and field-of-view half-angle θ_{fov} , is

$$\begin{aligned}
 P_{\tau}(\xi) &= \int_{r=0}^a \int_{\theta=0}^{\theta_{\text{fov}}} \int_{\phi=0}^{2\pi} I \cos \theta \sin \theta d\theta d\phi \\
 &= \frac{E_0}{4} e^{-\kappa \xi} (3 - \cos 2\theta_{\text{fov}} - 2 \cos^3 \theta_{\text{fov}}) \\
 &\quad \times \left[1 - \exp \left\{ - \frac{a^2}{2 [\sigma_x^2(\xi) + \sigma_B^2]} \right\} \right] A(\tau, \xi). \quad (65)
 \end{aligned}$$

For $a = \infty$, $\theta_{\text{fov}} = \pi/2$, $E_0 = 1$, and $\kappa = 0$, Eq. (65) reduces to $P_{\tau}(\xi) = A(\tau, \xi)$, consistent with the infinite-plane-receiver analysis in Sec. IV, p. 43.

PROPAGATION BELOW CLOUD

Consider the narrow delta pulse of light emerging from the cloud bottom ($z = \tau$) at position $\underline{r}' = (x', y')^T$, time ξ' , and direction $\alpha' = (\theta', \phi')$. At time $\xi = \xi' + d \sec \theta$, the pulse will illuminate the plane $z = \tau + d$ at the position $\underline{r} = \underline{r}' + d \tan \theta \underline{n}_{\perp}$ while maintaining the direction $\alpha = \alpha'$, where $\underline{n}_{\perp} = (\cos \phi', \sin \phi')^T$. Hence the atmospheric propagator from the plane $z = \tau$ to the plane $z = \tau + d$ is

$$G(\underline{r}, \tau + d, \alpha, \xi; \underline{r}', \tau, \alpha', \xi') \\ = e^{-\kappa d \sec \theta'} \delta(\underline{r} - \underline{r}' - d \tan \theta' \underline{n}_\perp) \delta(\alpha - \alpha') \delta(\xi - \xi' - d \sec \theta') .$$

In cartesian coordinates, the radiance emerging from the plane $z = \tau + d$ is given by

$$I(\underline{r}, \tau + d, \alpha; \xi) = \int_0^\infty d\xi' \int_{R^2} d^2 \underline{r}' \int_\Omega d\omega_{\alpha'} I(\underline{r}', \tau, \alpha'; \xi') G \\ = e^{-\kappa d \sec \theta} I(\underline{r} - d \tan \theta \underline{n}_\perp, \tau, \alpha; \xi - d \sec \theta) ,$$

which, with the help of Eqs. (61) and (64), becomes

$$I(\underline{r}, \tau + d, \alpha; \xi) = \frac{E_0}{4\pi} e^{-\kappa \xi} (2 + 3 \cos \theta) \rho_{\underline{r}}(\underline{r}, \xi) \\ \times A(\tau, \xi - d \sec \theta) , \quad 0 \leq \theta \leq \pi/2 , \quad (66)$$

where

$$\rho_{\underline{r}}(\underline{r}, \xi) = \frac{1}{2\pi [\sigma_x^2 (\xi - d \sec \theta) + \sigma_B^2]} \\ \times \exp \left\{ - \frac{(x - d \tan \theta \cos \phi)^2 + (y - d \tan \theta \sin \phi)^2}{2 [\sigma_x^2 (\xi - d \sec \theta) + \sigma_B^2]} \right\} . \quad (67)$$

The value of the radiance at $z = \tau + d$ and $\underline{r} = 0$ is of interest below. Hence, from Eq. (66),

$$I(\underline{r}, \tau + d, \alpha; \xi) \Big|_{\underline{r}=0} = \frac{E_0 e^{-\kappa \xi} (2 + 3 \cos \theta) A(\tau, \xi - d \sec \theta)}{8\pi^2 [\sigma_x^2 (\xi - d \sec \theta) + \sigma_B^2]} \\ \times \exp \left\{ - \frac{d^2 \tan^2 \theta}{2 [\sigma_x^2 (\xi - d \sec \theta) + \sigma_B^2]} \right\} . \quad (68)$$

For calculating the power into an on-axis receiver at $z = \tau + d$ with aperture a and field-of-view θ_{fov} , we assume that the radiance over the aperture is approximately equal to its value at $\underline{r} = 0$ when

$$a \ll [\sigma_x^2(\xi) + \sigma_B^2]^{\frac{1}{2}}$$

for all $\xi > \tau$. Thus, from Eq. (68), the received power is given by

$$\begin{aligned} P_{\tau+d}(\xi) &\cong \int_{|\underline{r}| < a} d^2 \underline{r} \int_{\theta=0}^{\theta_{fov}} d\theta \int_{\phi=0}^{2\pi} d\phi \left. I \right|_{\underline{r}=0} \cos \theta \sin \theta \\ &= \frac{E_0^2 a^2}{4} e^{-\kappa \xi} \int_{\theta=0}^{\theta_{fov}} \frac{A(\tau, \xi - d \sec \theta)}{\sigma_x^2(\xi - d \sec \theta) + \sigma_B^2} \\ &\quad \times \exp \left\{ - \frac{d^2 \tan^2 \theta}{2 [\sigma_x^2(\xi - d \sec \theta) + \sigma_B^2]} \right\} (2 + 3 \cos \theta) \cos \theta \sin \theta d\theta, \end{aligned} \quad (69)$$

which may be evaluated numerically. However, if θ_{fov} is also small, Eq. (69) reduces to

$$\begin{aligned} P_{\tau+d}(\xi) &= \frac{5a^2 E_0^2}{4d^2} e^{-\kappa \xi} A(\tau, \xi - d) \\ &\quad \times \left[1 - \exp \left\{ - \frac{d^2 \theta_{fov}^2}{2 [\sigma_x^2(\xi - d) + \sigma_B^2]} \right\} \right]. \end{aligned} \quad (70)$$

As a check for Eq. (70), we obtain

$$\lim_{d \rightarrow 0} P_{\tau+d}(\xi) = \frac{5a^2 E_0^2 \theta_{fov}^2}{8 [\sigma_x^2(\xi) + \sigma_B^2]} e^{-\kappa \xi} A(\tau, \xi),$$

which is identical to P_τ given by Eq. (65) evaluated with the usual approximations when a and θ_{fov} are assumed to be small.

To show the effect of replacing Eq. (69), which requires a numerical integration, with the closed-form equation (70), Fig. 15 plots

$$E_{\tau+d}(a, \theta_{\text{fov}}) = \int_{\xi=0}^{\infty} P_{\tau+d}(\xi) d\xi$$

against θ_{fov} using $P_{\tau+d}(\xi)$ from both Eqs. (69) and (70). The approximate equation (70) results in under a 5 percent error in $E_{\tau+d}(a, \theta_{\text{fov}})$ for $\theta_{\text{fov}} \leq 15$ deg when $E_0 = 1$ J, $\kappa = 0$, $\langle \cos \theta \rangle = \langle \cos^2 \theta \rangle = 0.850$, $\tau = 30$, $d = 150$, $\sigma_B = 500$, and $a = 0.01$. Therefore, we recommend the use of the computationally efficient Eq. (70) whenever $\theta_{\text{fov}} \leq 15$ deg. Furthermore, Fig. 15 indicates that beyond about $\theta_{\text{fov}} = 20$ deg, the signal energy into the receiver does not increase appreciably.

Figures 16 through 21 show the effect of the cloud and atmospheric layers on energy and pulse stretching for a finite receiver located on-axis a distance d below the cloud. In each case, the received energy is given by

$$E_{\tau+d}(a, \theta_{\text{fov}}) = \int_{\xi=0}^{\infty} P_{\tau+d}(\xi) d\xi ,$$

where $P_{\tau+d}(\xi)$ is computed from Eq. (69) if $\theta_{\text{fov}} > 15$ deg or from Eq. (70) if $\theta_{\text{fov}} \leq 15$ deg. Pulse stretching is again represented by the average multipath delay

$$\overline{\Delta \xi} = E_{\tau+d}^{-1}(a, \theta_{\text{fov}}) \int_{\xi=0}^{\infty} \xi P_{\tau+d}(\xi) d\xi - (\tau + d) .$$

We do not parameterize any calculations on receiver aperture because of the simple dependence of $P_{\tau+d}(\xi)$ on aperture a , as evinced in Eqs. (69) and (70). The following input values are used in the computations for Figs. 16 through 21: $E_0 = 1$ J, $\kappa = 0$, $\langle \cos \theta \rangle = \langle \cos^2 \theta \rangle = 0.850$, and $\sigma_B = 25$. The thickness of the atmospheric layer

is expressed in kilometers under the assumption of a mean free scattering length $k_s^{-1} = 20$ m; in this case, the standard deviation of the incident beam is 500 m.

Figures 16 and 17 show the interaction of atmospheric layer thickness and field of view. For thinner layers, wider fields of view increase both received energy and pulse stretching, but the latter effect is relatively slight. For thicker atmospheric layers ($D > 3$ km), increasing field of view beyond 20 or 30 deg does not influence received energy or pulse stretching--because, if the spot subtended by the receiver on the cloud bottom is larger than the main body of the exiting beam, then increasing field of view has little effect on the received pulse. Figures 18 through 21 display the relative importance of cloud as opposed to atmospheric layer thickness when the receiver field of view is fixed at 15 deg. With regard to received energy and especially multipath pulse stretching, the most important factor is the optical thickness of the cloud, not its distance above the receiver.

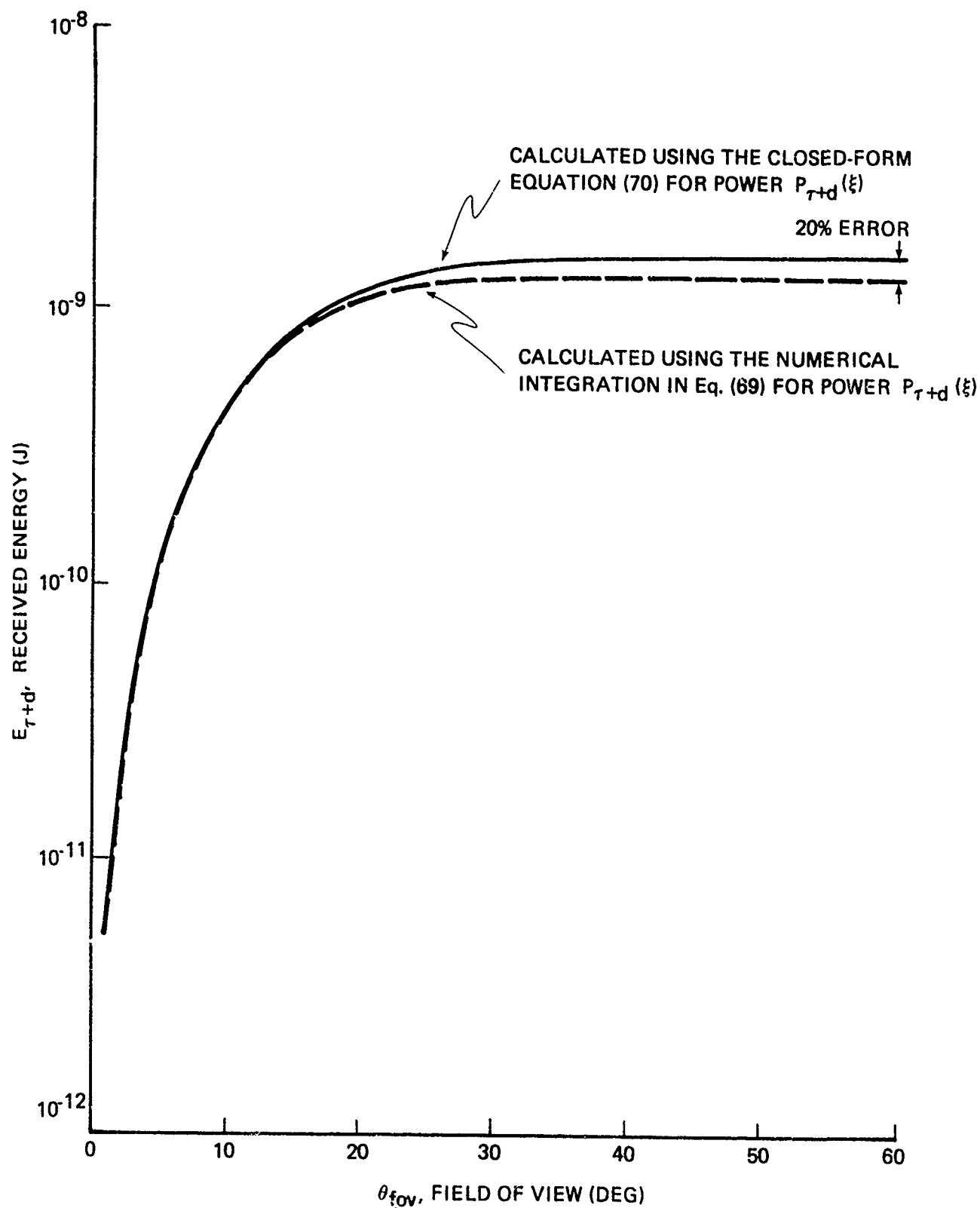


Fig. 15--Received energy versus field of view using a generally applicable expression and one restricted to small-field-of-view receivers

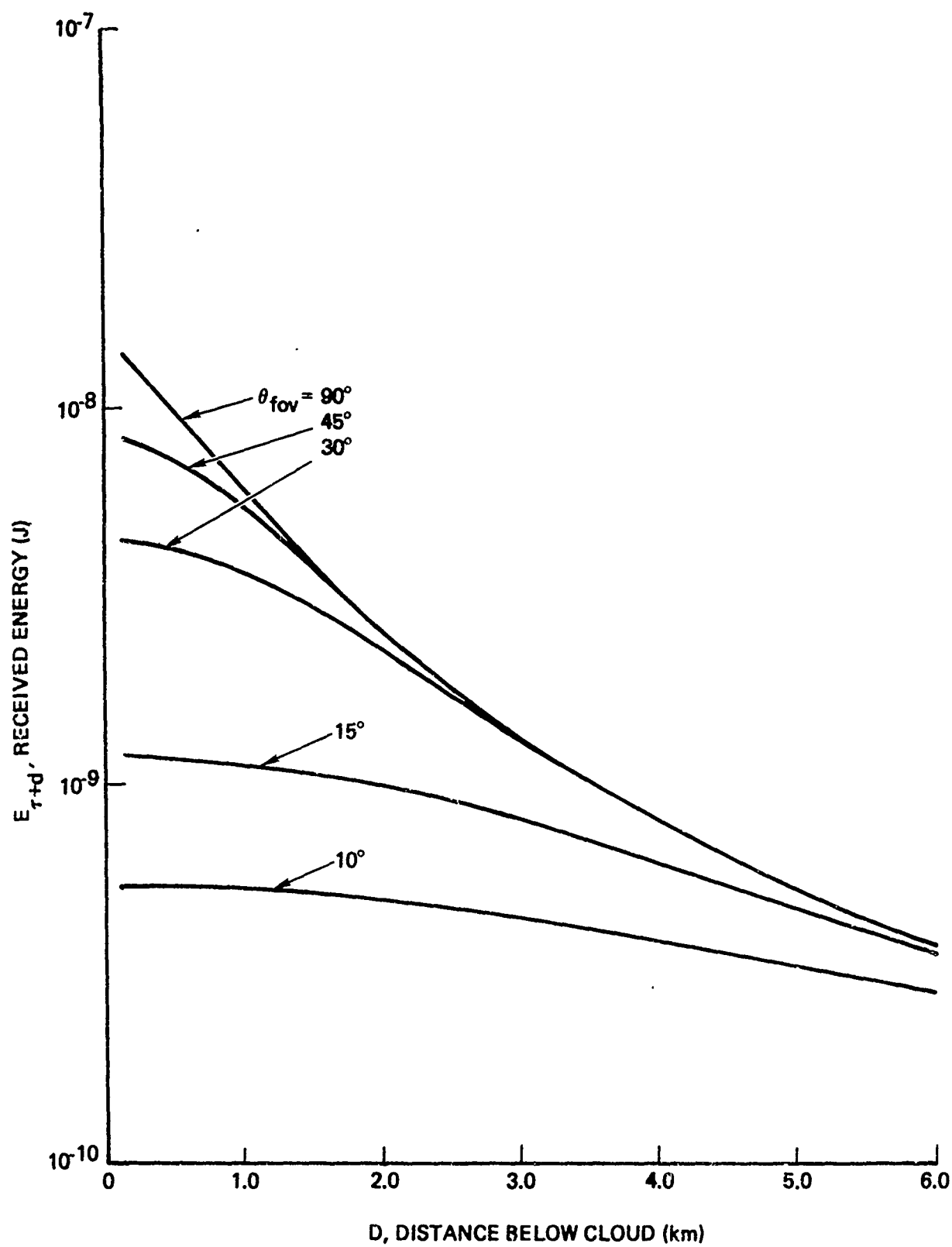


Fig. 16--Received energy versus distance below cloud for $\tau = 30$ and various receiver fields of view

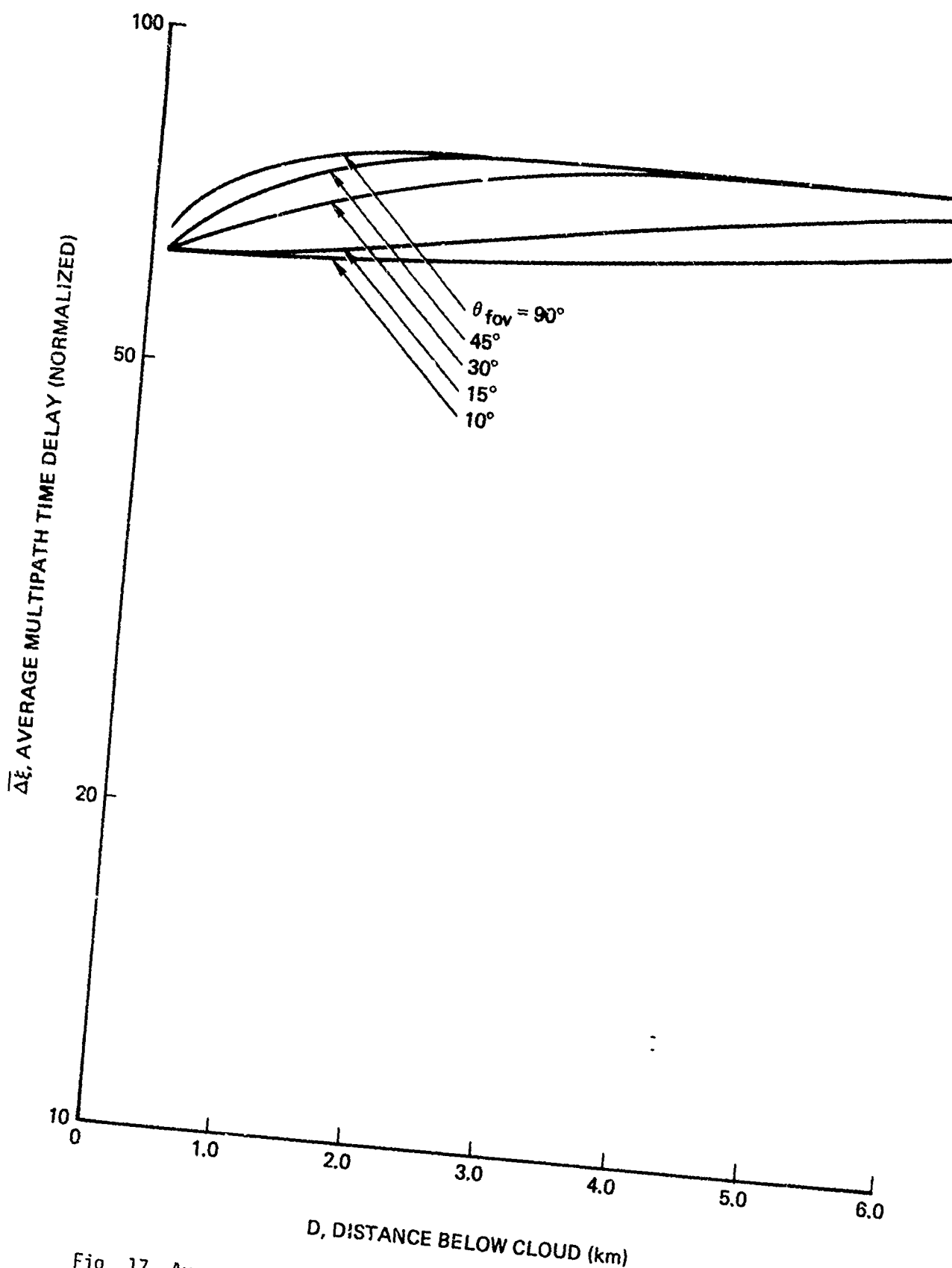


Fig. 17--Average multipath time delay versus distance below cloud for $\tau = 30$ and various receiver fields of view

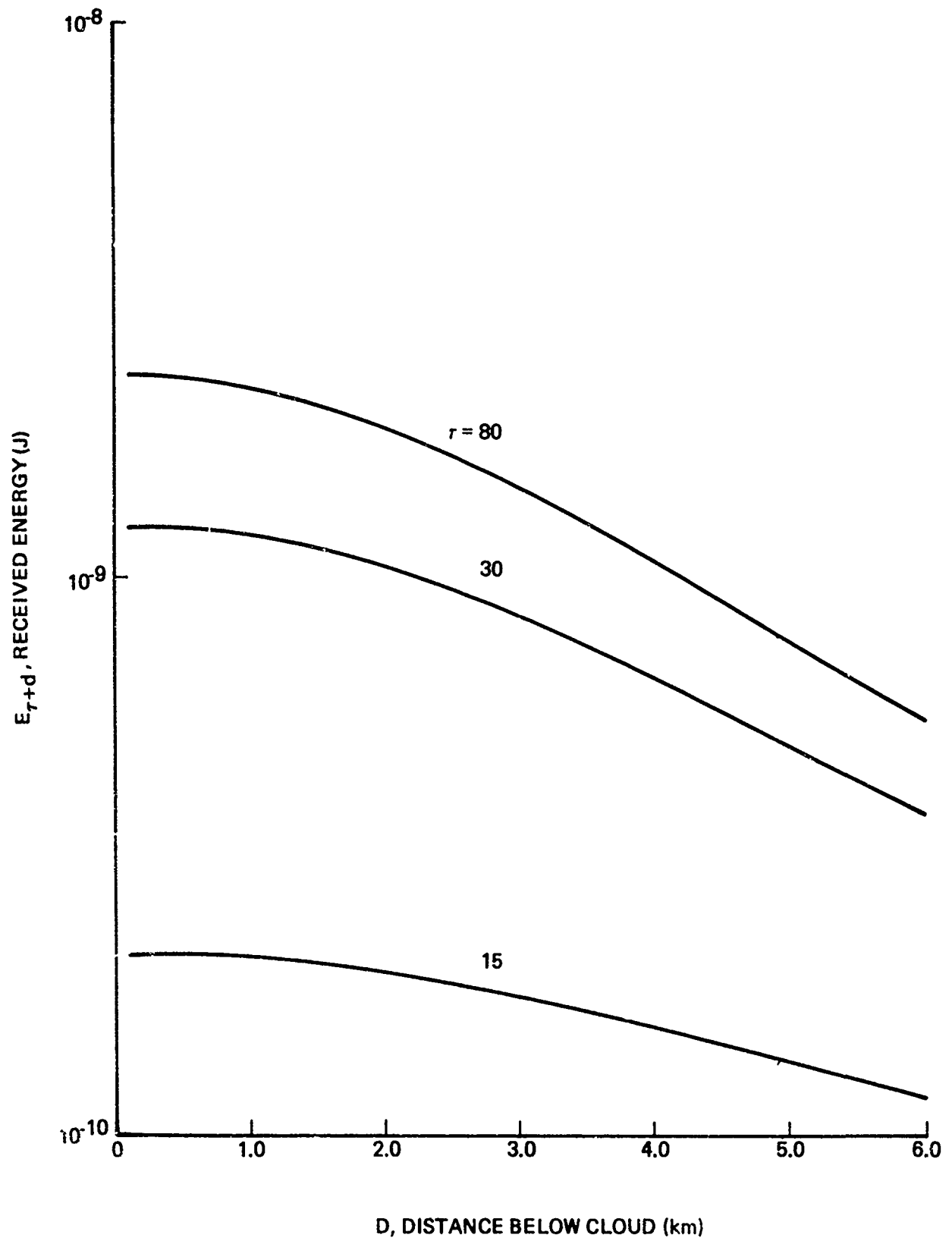


Fig. 18--Received energy versus distance below cloud for 15° field of view and various cloud thicknesses

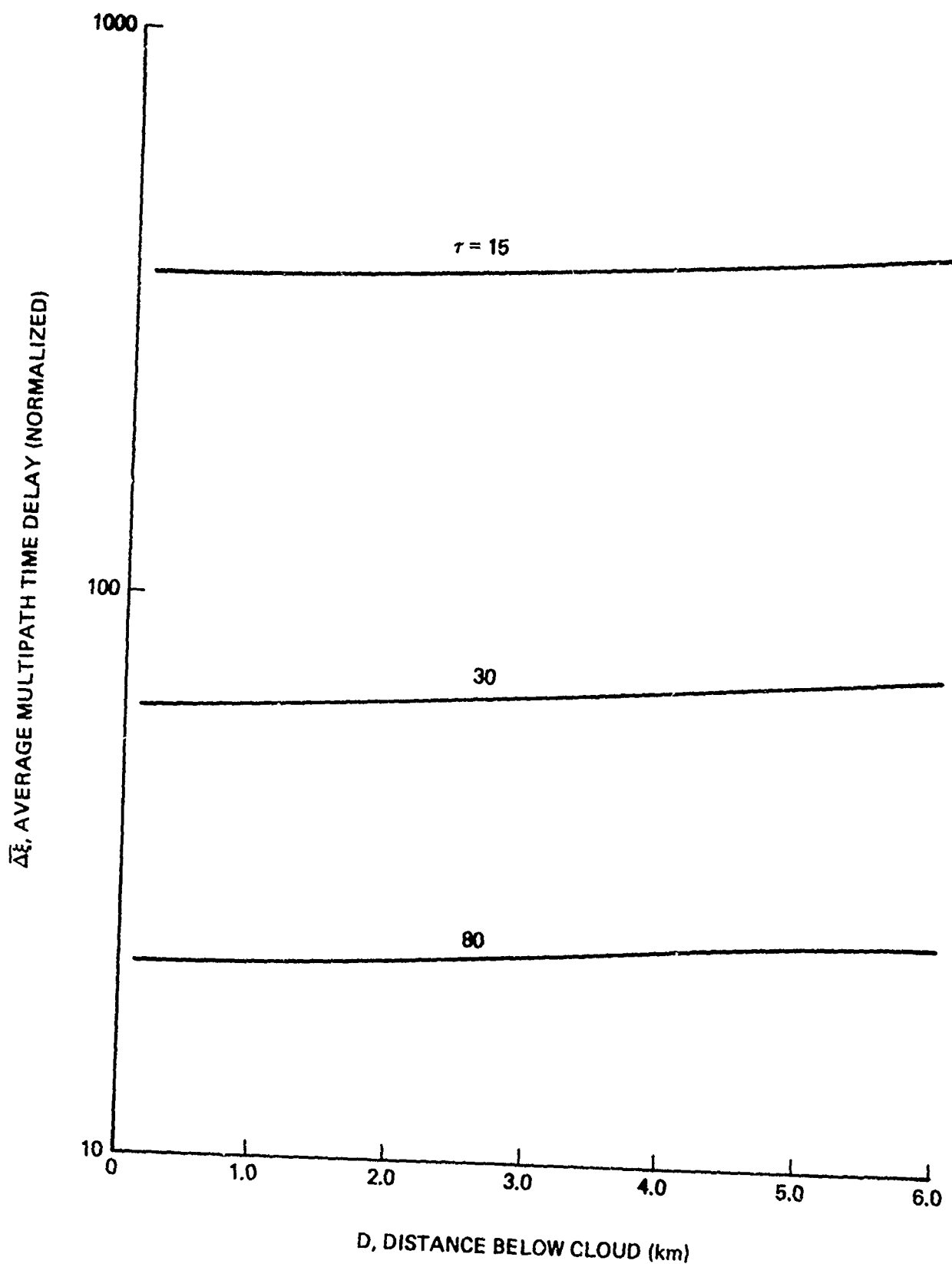


Fig. 19--Multipath time delay versus distance below cloud for 15° field of view and various cloud thicknesses

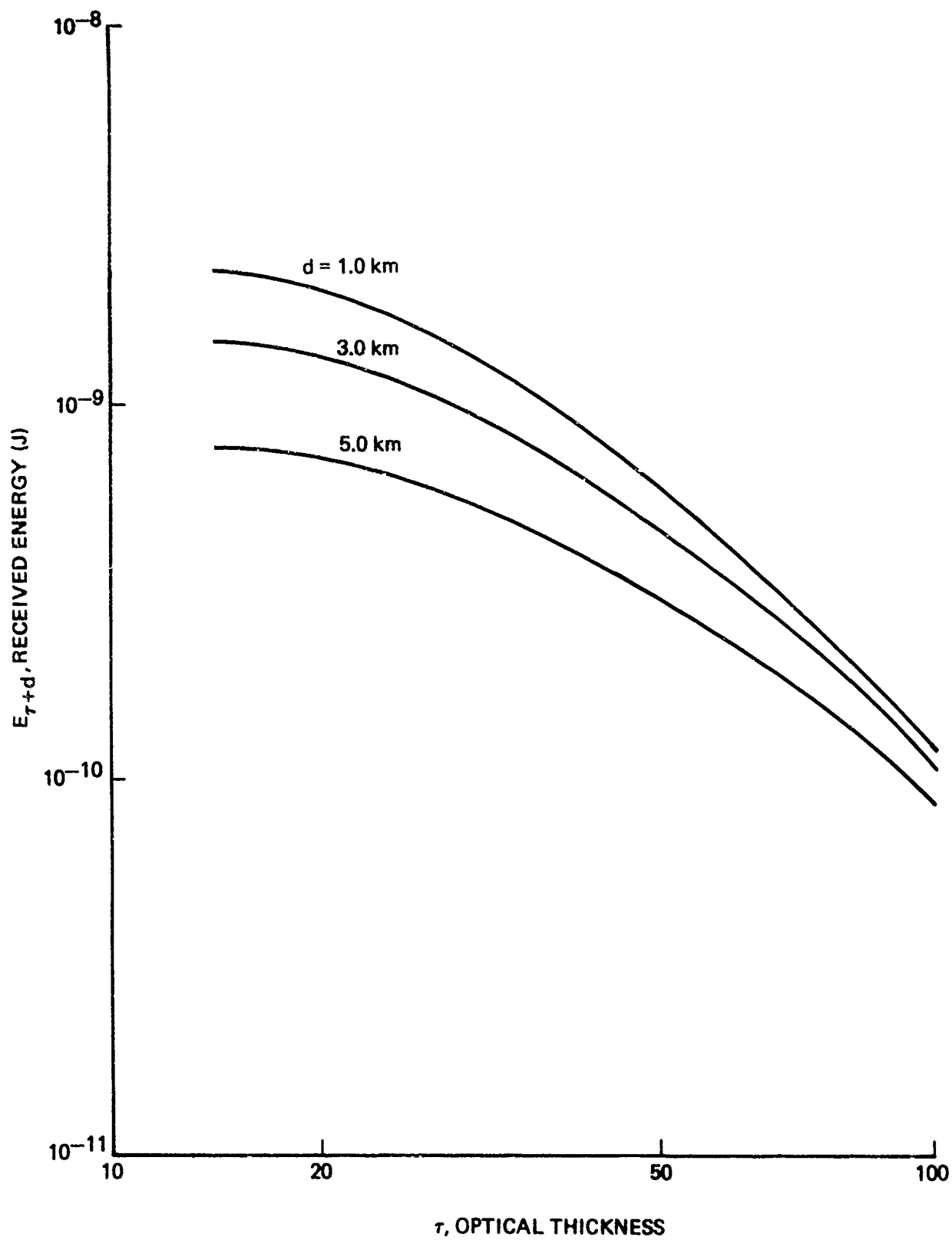


Fig. 20--Received energy versus optical thickness of cloud for 15° field of view and various receiver-to-cloud distances

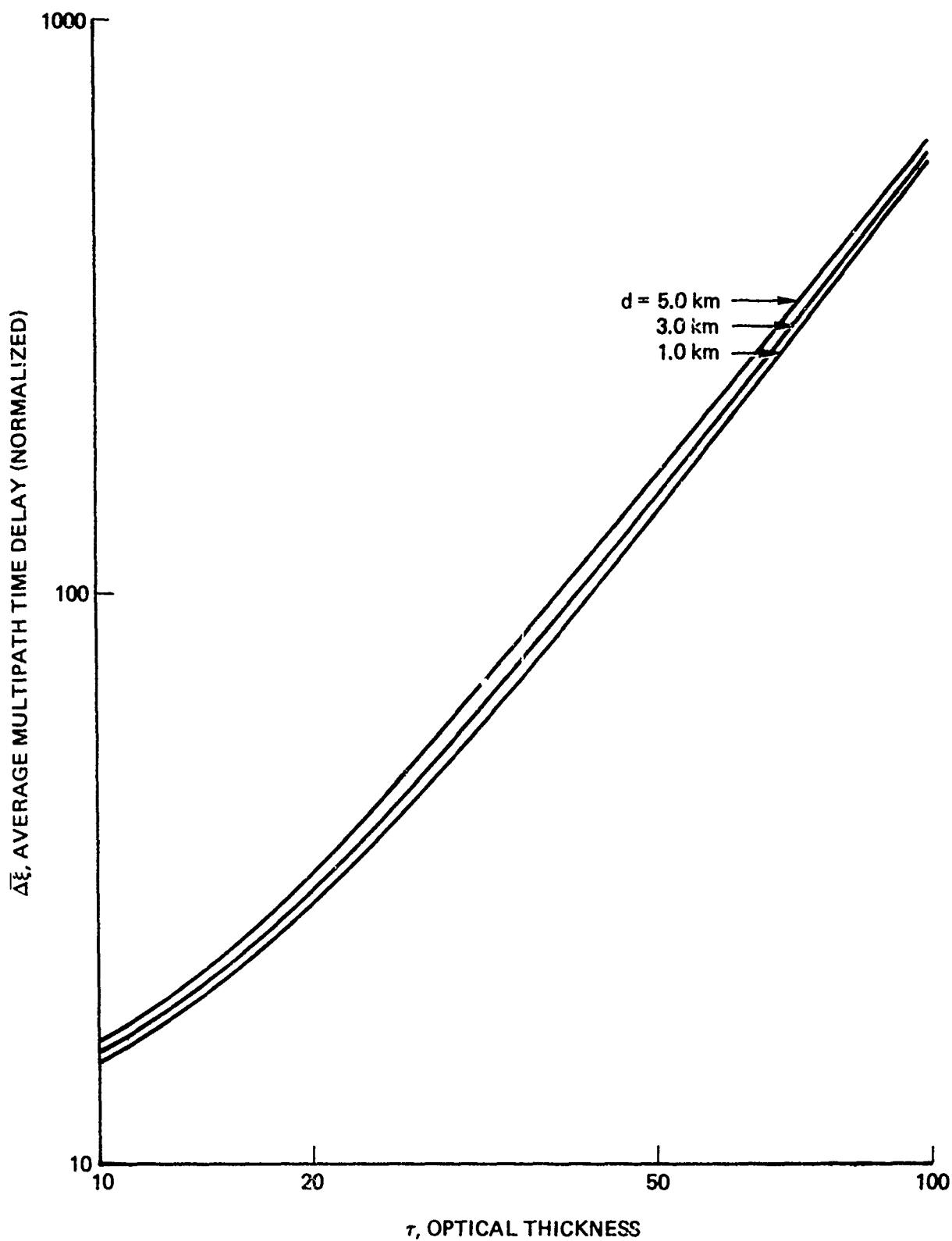


Fig. 21--Multipath time delay versus optical thickness of cloud for 15° field of view and various receiver-to-cloud distances

VI. IMPLICATIONS FOR BLUE-GREEN PROGRAM

It is difficult to assess the feasibility of satellite-to-submarine optical communications without a well-founded, tractable, analytic treatment for multiple scattering in clouds. Simulation results have been computationally expensive, highly aggregated (e.g., based on infinite receiving planes), and often presented without error bounds. Though for finite receivers, analyses involving the small-angle assumption are fundamentally problematical, especially when applied to all but the thinnest clouds.

The mathematical treatment of multiple scattering presented here begins by deriving the scattering moments--predicated on basic physical concepts and performed without approximations--and continues by developing the diffusion model, which was validated by published simulation results for the identical problems. The credibility of both the analytic model and the simulation is established by their remarkable agreement for optical thicknesses greater than 15--the range for which clouds most severely degrade the propagation path. However, the diffusion model provides expressions that are both computationally efficient and cover a broad range of problems at all levels of aggregation. The moment formulae and the diffusion expressions also provide the physical insight into the scattering process that may be required to resolve new problems and existing anomalies in certain experimental results, as discussed below.

Since the diffusion model provides an expression for the full radiance distribution on a plane just above the ocean surface, it can be linked with other models for radiance propagation through the ocean surface down to a submarine-mounted receiver. With the addition of noise, the full propagation path would be modeled, allowing efficient optimization of receiver aperture and field of view. In any case, we are now prepared to comment on relevant parts of the current model of optical pulse propagation from satellite to submarine.

NAVY MODEL

The Navy's blue-green single-pulse downlink propagation model [9] provides a common base for analyzing satellite-to-submarine communication system performance. The Navy model is modularized to permit convenient incorporation of new results for each part of the propagation path (e.g., clouds, atmosphere, air/water interface). The developments presented here are relevant to pulse shape and width, total transmission through clouds and the cloud-to-ocean atmospheric layer, and the angular distribution of exiting radiation below the cloud. In the following discussion, we either confirm the expressions used in the Navy model or suggest alternatives.

The Navy model represents energy transmission through the cloud layer by the Bucher simulation fit [4], which is given by

$$E_{\tau} = \frac{1.69}{\sqrt{\tau} + 1.42} \quad (71)$$

in our notation. Figure 12 plots Eq. (71) together with the diffusion model result. The close agreement between the two curves demonstrates that Eq. (71) is essentially correct and not subject to the factor-of-two error in the 1.69 and 1.42 constants suggested in Ref. 9. The extrapolation of Eq. (71) to $E_{\tau} = 1$ for $\tau = 0$, as done in the Navy model, seems appropriate; moreover, we agree with the zenith-angle dependence on signal transmission taken from Bucher.

The Navy model mechanism for cloud-to-water energy transmission appears to be inconsistent with the definition of energy transmission through the cloud embodied in Eq. (71). Indeed, energy transmission through the cloud can be defined as the probability that a photon entering the cloud from the top will eventually emerge from the bottom. Applied to energy transmission through the cloud-to-water atmospheric layer, this definition leads to the conclusion that transmission loss is due only to the angular distribution of exiting photons and the atmospheric absorption coefficient. Therefore, the diffusion model calculates the transmission loss as

$$\int_{\Omega} e^{-\kappa d \sec \theta} g(\alpha) d\omega_{\alpha} = \frac{1}{7} [4 + \kappa d(4 - 3\kappa d) Ei(-\kappa d) + 3e^{-\kappa d}(1 - \kappa d)] , \quad (72)$$

where the angular distribution $g(\alpha)$ is given by Eq. (62) and $Ei(x)$ is the exponential integral function [16]. Equation (S-6a) in Ref. 9 does not account for atmospheric absorption, is apparently based on a spot spreading phenomenon, assumes a Lambertian distribution of emerging light, and is substantially different from Eq. (72).

The received pulse shape given by $F(t) = t e^{-\kappa t}$ in Ref. 9 conforms well with those computed by Bucher [4] and hence with those computed here. For multipath time spreading due to clouds, we suggest use of the Bucher simulation fit

$$\overline{\Delta \xi} = \frac{0.62}{v} (\tau v)^{1.94} ,$$

which agrees with our results for all τ (Figs. 7 and 14). Equation (34), which is used in Ref. 9, is not recommended because it may not conform to physical prerequisites, as discussed in Sec. III. Figures 19 and 21 show that pulse stretching due to the cloud-to-water atmospheric path is negligible compared with that due to clouds. Hence we agree with Eq. (S-25b), which sets cloud-to-water pulse stretching to zero.

EXPERIMENTAL VERIFICATION

Because the diffusion model provides expressions for the power received by a finite aperture and field-of-view receiver [Eqs. (69) and (70)] located an arbitrary distance below a given cloud layer, the model is suitable for verification by comparison with experimental results. Indeed, an experiment is currently under way on the island of Kauai partly for this purpose. However, experimental verification is fraught with complications, such as (1) the difficulty of measuring experimental input parameters (e.g., τ , $\langle \cos \theta \rangle$, k_a) accurately enough to conclude that the model is correct, and (2) the inconsistency of the geometric boundaries governing the experiment with the assumptions

used to develop the model (e.g., a plane-parallel cloud layer). Obtaining accurate measurements of physical parameters is beyond the scope of this report, but the effect of boundary problems is discussed below.

One important, recent multiple scattering experiment was the Naval Ocean Systems Center (NOSC) work on fog propagation reported in Ref. 1. The effect of the ground as an absorbing boundary for photons has been of some concern in interpreting the results of the NOSC experiment. By using the boundary value techniques discussed in Sec. IV, the diffusion model can be extended to account for an absorbing plane parallel to and laterally displaced from the axis of propagation. Similar extensions can be developed to model rectangular clouds, or rectangular slots or holes in clouds.

A scaled-down multiple scattering laboratory experiment has been suggested, using large tanks filled with water and suspended oil droplets. The dimensions of the tank and the absorptive properties of the walls required to model a cloud without horizontal boundaries are two of the technical issues that should be resolved before such an experiment is undertaken. Our results indicate that tank boundaries (perpendicular to the coordinate frame of photon motion) can be modeled in the diffusion theory sense, as either absorbing, reflecting, or elastic, so long as photons enter the tank at least 15 optical thicknesses from the side walls. Thus, the tank dimensions and side-wall absorptive properties may not inhibit the laboratory verification of the diffusion model.

REFERENCES

1. Mooradian, G. C., et al., "Blue-Green Pulsed Propagation through Fog," *Applied Optics*, Vol. 18, No. 4, 15 February 1979, pp. 429-441.
2. Chandrasekhar, S., *Radiative Transfer*, Oxford at the Clarendon Press, Oxford, 1950.
3. Stotts, L. B., "The Radiance Produced by Laser Radiation Transversing a Particulate Multiple-Scattering Medium," *J. Opt. Soc. Am.*, Vol. 67, No. 6, June 1977, pp. 815-819.
4. Bucher, E. A., "Computer Simulation of Light Pulse Propagation for Communication through Thick Clouds," *Applied Optics*, Vol. 12, No. 10, October 1973, pp. 2391-2400.
5. Parzen, E., *Stochastic Processes*, Holden-Day, San Francisco, 1962.
6. Reif, F., *Statistical Thermal Physics*, McGraw-Hill, New York, 1965.
7. Arnush, D., "Underwater Light-Beam Propagation in the Small-Angle-Scattering Approximation," *J. Opt. Soc. Am.*, Vol. 62, No. 9, September 1972, pp. 1109-1111.
8. Stotts, L. B., "Closed Form Expression for Optical Pulse Broadening in Multiple-Scattering Media," *Applied Optics*, Vol. 17, No. 4, 15 February 1978, pp. 504-505.
9. Technical Advisor to the Blue-Green Optical Communication Program Joint Coordinating Committee, *Naval Blue-Green Single-Pulse Downlink Propagation Model*, Naval Ocean Systems Center, San Diego, Calif., TR 387, 1 January 1979.
10. Feller, W., *An Introduction to Probability Theory and Its Applications*, Vol. 2, Wiley, New York, 1966.
11. Morse, P., and H. Feshbach, *Methods of Theoretical Physics*, McGraw-Hill, New York, 1953.
12. DeGroot, J. S., R. M. Frank, and H. S. Stewart, *Effects of Clouds on X-Ray Induced Fluorescent Light from a Nuclear Burst in Space*, E. H. Plesset Associates, Santa Monica, Calif., C73-65(u)11, 29 January 1965.
13. Fritz, S., "Scattering and Absorption of Solar Energy by Clouds," Ph.D. Thesis, Massachusetts Institute of Technology, Cambridge, 1953.

PRECEDING PAGE BLANK-NOT FILMED

14. Carslaw, H. S., and J. C. Jaeger, *Conduction of Heat in Solids*, 2d ed., Oxford at the Clarendon Press, Oxford, England, 1959.
15. Ciany, C., G. Schroeder, and G. Lee, "Optimum System Design for Optical Satellite to Submarine Communication Links," McDonnell-Douglas Astronautics, St. Louis, Mo. (unpublished).
16. Gradshteyn, I. S., and I. M. Ryzhik, *Table of Integrals, Series, and Products*, 4th ed., prepared by Yu. V. Geronimus and M. Yu. Tseytlin, translation edited by Alan Jeffrey, Academic Press, New York, 1965.